Energy & Buildings 319 (2024) 114512

Contents lists available at ScienceDirect

Energy & Buildings

journal homepage: www.elsevier.com/locate/enb

Dynamics of thermal plumes for large spaces: A comparative study of in-situ smoke test and a CFD model

Rafaela Mateus [a,b,*], Armando Pinto [b], José M.C. Pereira [a]

[a] LAETA, IDMEC, Instituto Superior Técnico, Universidade de Lisboa, Mechanical Engineering Department/LASEF, Av.Rovisco Pais, 1, Lisbon 1049-001, Portugal
[b] NAICI, Laboratório Nacional de Engenharia Civil, Buildings Department, Av. do Brasil 101, 1700-075 Lisboa, Portugal

ARTICLE INFO

Keywords:
Flow Visualization
Thermal plume
Smoke Test
CFD
Passive Scalar
Natural ventilation

ABSTRACT

This study focuses on natural convection heat transfer in building heating and ventilation. Amid advancements in natural ventilation and a changing energy landscape, innovative heating methods are crucial. Thermal radiators play a key role in enhancing heat convection and understanding thermal plumes to optimize heating efficiency.

This study investigates the use of coloured smoke sources to visualize thermal plume flow fields in real-scale (in-situ), naturally ventilated large spaces, distinguishing itself from most studies that prioritize enhancing thermal efficiency radiator. It offers a way for both qualitative and quantitative validation of a CFD model using passive scalars and experimental images to illustrate thermal plume propagation. This novel approach provides an effective way to visualize and understand thermal plumes in spaces where other experimental techniques are challenging to implement.

Experimental results showed high consistency between measured and CFD values for velocity, temperature, and heat exchange, with differences below 10 %. The study unveiled a low impact of initial smoke source velocities on plume visualization. Using coloured smoke images to validate the CFD model yielded errors from 2.3 % to 14.5 %, proving the method's reliability for both qualitative and quantitative analysis of plume propagation, offering valuable insights into air propagation in naturally ventilated spaces.

1. Introduction

The study of heat transfer through natural convection holds significant relevance in various engineering domains, particularly in the context of heating and ventilating buildings, as well as in heat exchange processes [1]. Over the years, significant advancements have been made in the field of natural ventilation [2,3]. This progress is instrumental not only in enhancing the energy efficiency of existing structures but also in elevating indoor air quality (IAQ), especially in the context of conventional buildings and Nearly Zero Energy Buildings (NZEB) [4].

In a world grappling with climate change, the energy landscape is evolving significantly. This shift not only calls for innovative heating solutions but also demands concerted action to tackle global energy poverty. Eurostat's January 2020 data revealed that around 6.9 % of the EU population faced high energy poverty rates [5]. Energy poverty involves the inability to access sufficient energy services, driven by factors like low income, poor housing conditions, and rising energy costs. Inadequate heating can cause discomfort and health issues for occupants, while also leading to condensation problems due to insufficient ventilation practices [6].

Thermally driven natural ventilation, governed by indoor-outdoor temperature differences, is an energy-efficient strategy [7,8]. Utilizing thermal plume effects offers efficient cooling solutions for buildings with large air volumes (large spaces) [9,10]. Strategic deployment of thermal radiators can address heating challenges while upholding energy efficiency goals [11]. Research in thermal radiator systems focuses on enhancing energy efficiency and ensuring proper air distribution, particularly through generating thermal plumes [12,13]. These plumes, associated with convective motion from localized heat sources, play a significant role in both confined and unconfined spaces [14]. Their characteristics, including detachment from heat sources and nonlinear behaviours, are studied using numerical methods and experiments [14,15].

A comprehensive understanding of the dynamics and characteristics of thermal plumes is essential for optimizing heating efficiency and ensuring that heat distribution meets the requirements and expectations

* Corresponding author at: LAETA, IDMEC, Instituto Superior Técnico, Universidade de Lisboa, Mechanical Engineering Department/LASEF, Av.Rovisco Pais, 1, Lisbon 1049-001, Portugal.
E-mail address: rafaela.mateus@tecnico.ulisboa.pt (R. Mateus).

https://doi.org/10.1016/j.enbuild.2024.114512
Received 31 March 2024; Received in revised form 12 June 2024; Accepted 3 July 2024
Available online 5 July 2024

of occupants. Most studies in the literature primarily focus on providing and analysing methods to enhance thermal efficiency, with a particular emphasis on examining changes in the geometry of the radiator's convector to increase the surface area for heat transfer [11,16–23]. Other factors such as flow type, connection methods, positioning, and radiation are also considered, albeit to a lesser extent [24–30].

However, the exploration of internal flow dynamics within spaces equipped with both heat exchangers and heat sources has been a relatively understudied area in the existing literature [31–33]. Conversely, research into buoyancy-driven ventilation in spaces featuring a single heat source or two heat sources has been more prevalent, albeit often in the context of scaled-down models [7].

Several investigations have delved into the dynamics of plumes above two or three heat sources within ventilated buildings. Notably, Cenedese and Linden [34] formulated a comprehensive model for the total volume flow and drag of two interconnected turbulent axisymmetric plumes. Additionally, several authors [35–39] have turned to Computational Fluid Dynamics (CFD) techniques to scrutinize the intricate behaviour of thermal plumes. Yin et al. [40–42] undertook a detailed examination of the influence of heat source spacing on flow dynamics in the immediate vicinity. They successfully derived a Gaussian curve fit describing plume velocity between three distinct heat sources situated at varying distances. Furthermore, Gao et al. [43] developed and validated a formula for calculating thermal stratification height in the presence of two turbulent buoyant plumes of equal intensity within a confined space. These studies have predominantly relied on theoretical methods or CFD simulations, underscoring the pivotal role of experimental approaches in visualizing plume propagation.

Experimentally, thermal plumes can be characterized by measuring various parameters using either individual or combined approaches. This includes techniques such as smoke visualization and Schlieren visualization to observe flow patterns, thermography for mapping temperature distribution, air velocity measurements using anemometers, and the use of temperature sensors to measure temperature variations. Numerically, the thermal plumes from a radiator can be analysed through computational simulations using Computational Fluid Dynamics (CFD). This involves creating a three-dimensional model of the radiator, defining initial and boundary conditions, selecting suitable turbulence models, and simulating the airflow around and within the radiator while considering heat transfer effects. Nevertheless, it is essential to consider the scale of the domains being studied and the necessity of employing simplified models to predict thermal plumes accurately.

Flow visualization remains an active area of research, with numerous techniques for interactive exploration of flow phenomena developed [44]. Smoke tests are visual experiments or techniques used to study the behaviour of fluid flow, making flow patterns visually more discernible and enabling an understanding of how heat is distributed within the environment. They typically involve the use of a tracer substance such as smoke, coloured dye, or small solid particles, which are introduced into the fluid to facilitate the visualization and analysis of the flow. Often, smoke originates from linear structures (e.g., a burning stick) or is introduced from specific points (smoke nozzles) [44]. As the fluid moves, these tracking particles or smoke reveal flow patterns, demonstrating how the fluid behaves around an object or in a specific configuration. These tests can be conducted in laboratories using small-scale models or in the field under uncontrolled conditions. Another prevalent technique in experimental flow visualization is the use of wool tufts, where small yarns are affixed to a surface and observed during flow experiments.

These types of tests not only offer the ability to visualize the movement of convection currents but also provide the capability to identify issues in heat distribution, verify airflow, and determine the direction of hot air, all with the aim of optimizing energy efficiency in the system. Furthermore, these tests aid in validating computational simulation models, enhancing predictions, and ensuring effective and cost-efficient heating in various environments.

Over time, several techniques and methods for visualizing smoke in fluid dynamics research have been proposed. In one approach, presented by N. Gao and Liu [45], an enhanced smoke-wire flow visualization technique was introduced, employing a large capacitor as its power source. Similarly, in the work of Funck et al. [44], an alternative representation of smoke was suggested, involving the use of a semi-transparent streak surface. However, it is important to note that their current implementation has certain limitations. Specifically, it is constrained to regular grids and demands the complete time-dependent dataset to be stored in the main memory. It is worth mentioning that these limitations are not unique to smoke visualization techniques but rather represent general challenges encountered in interactive visualization software.

In a study by Bangalee et al. [46], experiments investigated fluid-driven natural cross-ventilation using a scaled model in a uniform water channel flow. Flow visualization involved injecting food dye through a capillary tube, alongside PIV measurements and CFD calculations. While many studies have explored smoke application, particularly in fire propagation contexts [47–54], few have focused on experimental trials [51,54], and fewer still have employed full-scale models [46]. Jiao et al. [48], conducted full-scale tests following standardized methods, including the Chinese Standard GA/T 999–2012 and the Australia Standard AS4391-1999. Additionally, experimental studies in aerodynamic sealing of air curtains for particulate matter have been identified. Viegas et al. [55], conducted full-size experiments in the final phase, preceded by initial small-scale model tests with water as the working fluid.

It is important to highlight that in the study by Yang et al. [7], Schlieren visualization was employed to examine the characteristics of intersecting and trailing plumes (from 3, 4, and 5 sources) and the thermally stratified flow pattern. However, it is noteworthy that the Schlieren technique typically necessitates controlled conditions and a meticulously designed experimental setup to ensure accurate results. This is because it operates by detecting variations in light refraction as it traverses regions of varying density within the fluid.

In the context of CFD modelling, there are two primary methods for representing smoke: particles and passive scalars presented volumetrically to depict substance concentration, such as smoke. Particle-based approaches typically require a substantial number of particles to accurately represent smoke characteristics. On the other hand, passive scalars are scalar quantities that remain inert and do not actively impact fluid dynamics within the CFD simulation. This occurs when the source of the passive scalar can be considered as a fluid with contaminants or species present at minimal concentrations, transported alongside the fluid flow, and exerting negligible influence on the thermophysical properties of the fluid.

Given that existing studies mainly concentrate on enhancing thermal efficiency, this study aims to assess the possibility of employing coloured smoke sources for visualizing thermal plume flow fields in real-scale (in-situ), naturally ventilated environments. It also aims to establish qualitative and quantitative validation for a CFD model using passive scalars to illustrate the propagation of the thermal plume, based on experimentally obtained images. This approach provides an efficient means of visualizing and comprehending thermal plumes, particularly in large-scale naturally ventilated spaces where other experimental techniques are challenging to implement. Leveraging experimental images of coloured smoke enhances the accuracy and utility of CFD models, addressing the inherent challenges in visualizing and validating thermal plumes in full-scale naturally ventilated spaces.

2. Methodology

In this research paper, colour smoke visualization was employed to conduct a visual experiment involving multiple plume flows within a naturally ventilated environment. These experiments were conducted in uncontrolled conditions, aiming to showcase the applicability of this approach in full-scale models of spaces with large air volumes. Furthermore, the study sought to contribute to the qualitative and quantitative validation of CFD models.

2.1. Theoretical concepts of thermal plume interaction

Turbulent plume analysis relies on the classical point source theory, where plume self-similarity is a key concept. In this framework, both mean vertical velocity profiles and temperature profiles within a turbulent plume are modelled as Gaussian distributions. For a single plume originating from a point source in a uniform free environment, the plume's volume flow can be described by Eq. (1) [43].

$$Q = C_0\left(B_0 z^5\right)^{\frac{1}{3}} \tag{1}$$

where Q is the plume volume flow [m^3/s], $C_0 = \frac{6}{5}\alpha\left(\frac{9}{10}\alpha\right)^{\frac{1}{3}}\pi^{\frac{2}{3}}$ is the universal constant of the thermal plume, based on the entrainment constant α, B_0 is the buoyancy flux at the point source [m^4/s^3], and z is the vertical distance from the heat source [m].

Within a chamber featuring openings at both its upper and lower sections, commonly referred to as the "emptying filling box model," research conducted by Linden et al. [56] revealed the development of a two-layer stratification characterized by a horizontal interface situated between these layers. The dimensionless height ξ of this horizontal interface within an enclosure of height H is calculated using Eq. (2) [56]:

$$\frac{A}{H^2} = C_0^{\frac{2}{3}}\left(\frac{\xi^5}{1-\xi}\right)^{\frac{1}{2}} with \xi = \frac{h}{H} \tag{2}$$

where A is the effective area of the upper and lower openings of the enclosure [m^2], H is the height difference between the upper and lower openings [m], and h is the height of the interface [m] [56,57]. The constant C_0 is identical to the constant employed in Eq. (1).

In the scenario involving two plumes of equal intensity, the total volume flux is determined by Eq. (3) [7,34,56]. As indicated in the study conducted by Cenedese and Linden [34], the space above the two plume sources can be subdivided into three distinct regions, as depicted in Fig. 1. In Region 1, each plume operates independently. In Region 2, the two plumes come into contact, leading to a deviation from the Gaussian profiles characterizing the average buoyancy of a single plume. Finally, in Region 3, the two plumes merge to form a unified plume, and Gaussian profiles can once again be applied for characterization [43].

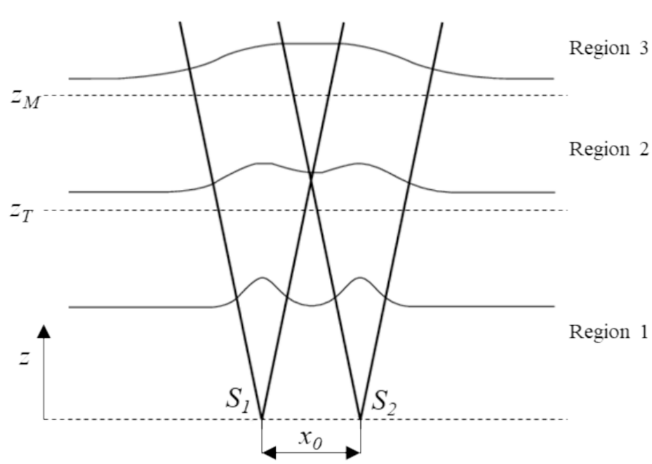

Fig. 1. Schematic illustration depicting two interacting buoyant plumes of equal intensity, with three delineated regions illustrating the evolution processes.

$$Q = 2\left(\frac{9}{10}\alpha_{eff}\right)^{\frac{1}{3}}\frac{6}{5}\pi^{\frac{2}{3}}\alpha_{eff}B_0^{\frac{1}{3}}z^{\frac{5}{3}} = 2C_{eff}B_0^{\frac{1}{3}}z^{\frac{5}{3}} \tag{3}$$

where $B_0 = g'Q_0$ is the buoyancy strength [m^4/s^3], $g' = g(\rho_p - \rho_a)/\rho_0$ is the reduced gravity of the plume [m/s^2], g is the gravitational acceleration [m/s^2], ρ_p is the density of the plume [kg/m^3], ρ_a is the uniform ambient density [kg/m^3], ρ_0 is a reference density [kg/m^3], and Q_0 is the volume flux of each plume with origins at the same height [m^3/s]. The parameter α_{eff} represents an effective entrainment constant, expressing the overall volume flux variation as the process evolves. Detailed calculations for each region can be found in the study by Cenedese and Linden [34].

Inside an enclosure where two interacting plumes coexist, these plumes, emanating from separate heat sources, engage in mutual interaction and eventual amalgamation, as elucidated earlier. In a stable thermal setting, the cumulative buoyancy flux of these plumes remains invariant and is equivalent to the summation of the individual buoyancy fluxes at their respective sources. The volume flux entering or leaving the enclosure in a steady state can be precisely represented using Eq. (4) [43,56].

$$Q_P = A\sqrt{G'(H-h)} \tag{4}$$

where G' is the reduced gravity in the region above the interface and outside the plume [m/s^2]. For plumes in a thermal environment devoid of additional heat input, G' is equal to g' at the interface height due to a heat balance for the upper layer in a steady condition. The effective area (A) of both the top and bottom openings of the enclosure can be determined using Eq. (5) [56].

$$A = \frac{c_d A_{in} A_{out}}{\left[\frac{1}{2}\left(\frac{c_d^2}{c}{A_{in}}^2 + {A_{out}}^2\right)\right]^{\frac{1}{2}}} \tag{5}$$

where A_{in} and A_{out} are the areas of the bottom and top openings respectively [m^2], c is the pressure loss coefficient and c_d is the discharge coefficient.

In this investigation, the heat sources under consideration are vertical thermal radiators. The estimation of heat output from these vertical surface heat sources can be achieved using Eq. (6). This formula relies on the temperature difference in water enthalpy between the inlet and outlet sections of the vertical surface heat sources, in addition to the rate of water flow passing through the radiators. The calculation of the vertical surface heat sources' excess temperature above the indoor air temperature was determined through the use of Eq. (7) [58], while Eq. (8) was employed to describe the process of heat transfer via convection, adhering to Newton's law of cooling. Further calculations involved determining the radiant heat output from the vertical surface heat source into the room space (Eq. (9)) and towards the back wall (Eq. (10)) [59].

$$Q = \dot{m}(h_i - h_o) \tag{6}$$

where $\dot{m}$ is the water mass flow rate [kg/s], h_i and h_o are the water enthalpy [J/kg] at the inlet and outlet, respectively. The enthalpies were acquired by referring to thermodynamic tables [60].

$$\Delta T = \frac{T_i + T_o}{2} - T_r \tag{7}$$

where T_r is the room air temperature, T_i and T_o are the inlet and outlet water temperatures, respectively [°C].

$$Q_{convection} = hA(T_s - T_r) \tag{8}$$

where $Q_{convection}$ is the convective heat rate transferred through the exposed surface of the vertical surface heat source [W], T_s is the surface temperature of the vertical surface heat sources [°C], h is the convective coefficient which is a function of the fluid flow, fluid thermal properties, physical geometry and direction in space of the system that exhibits convection [W/m^2 °C], and A is the total surface area of the vertical surface heat sources [m^2].

The method employed for calculating the frontal surface temperature (T_s) of a vertical surface heat source involved computing the average temperature from a limited set of temperature measurements. Since the convection coefficient fluctuates with the height of the vertical surface heat source and is influenced by the precise measurement location of air temperature, an averaged convection coefficient was frequently utilized.

$$Q_{radiation1} = A\xi_{rad}\sigma\left(T_s^4 - T_r^4\right) \quad (9)$$

$$Q_{radiation2} = A\xi_{rad-w}\sigma\left(T_s^4 - T_r^4\right) \text{ with } \xi_{rad-w} = \left(\frac{1}{\xi_{rad}} + \frac{1}{\xi_w} - 1\right)^{-1} \quad (10)$$

where σ is the Stefan–Boltzmann constant (5.6703 × 108 W/m^2 K^4), A is the radiator frontal surface area (m^2), ξ_{rad} is the radiator emissivity, ξ_{rad-w} is the radiator-back wall emissivity, and ξ_w are the emissivity of the wall.

2.2. Experimental setup

The experimental configuration of the heating system comprised several components: a water heater tank responsible for storing and heating water, a circulating pump for distributing heated water throughout the system, a flow meter to measure water flow rate, a filling unit for convenient system replenishment, two vertical surface heat sources each equipped with 8 elements, insulated pipes to minimize heat dissipation, and associated accessories. The TBOE (Top and Bottom Opposite End) connection method was employed for each radiator, allowing water to flow in from the top and return from the bottom, positioned at opposite ends of the vertical surface heat source. This design ensured thorough water circulation within the radiator, optimizing its efficiency. Fig. 2 provides a schematic representation of the experimental setup, depicting the hot water circuit in red, the return circuit in blue, and the cold-water circuit in green. The vertical surface heat sources were positioned 110 mm away from the wall, fixed 500 mm above the floor, with a gap of 1 068 mm from the left-side column and a separation of 260 mm between the vertical surface heat sources.

The setup was located at LNEC, Lisbon, Portugal, within the testing area, operating under ambient conditions without controlled temperature and humidity. The testing space has dimensions of 14 700 mm width, 10 000 mm height, and 29 000 mm length. Multiple test segments are present within this space, and the facility is positioned between two columns on a wall with a beam at around 3 500 mm height.

The radiators (Fig. 3-a) utilized in the experimental setup were diecast and extruded aluminium radiators with 8 elements, coloured white. The characteristics of one element are detailed in Table 1 and were determined in accordance with the EN 442 standard [58].

For smoke tests, technical smoke sources of two colours, red and blue, were used to identify the thermal plume of each radiator and their interaction. These smoke sources are characterized by dimensions of 120 × 50 × 50 mm^3 and an average duration of 90 s, and their placement was done in accordance with the details provided in Fig. 3-b.

2.2.1. Measurement's equipment

S18B20 thermocouples were utilized to gauge both inlet and outlet temperatures, while a data logger designed for tracking humidity and temperature was employed to oversee room temperature and relative humidity in the ambient conditions. The monitoring of these measurements was managed by a Raspberry Pi, supported by a Python program specifically crafted for signal data processing.

For the determination of air velocity and temperature above the radiators, thermo-anemometers equipped with hot wire probes were deployed. Additionally, the assessment of surface temperature distribution (T_s), on the radiators was carried out using a thermal camera (emissivity of 0.9).

In smoke tests, concentrations were also monitored using MQ2 smoke sensors, and three cameras were employed to record the development of the thermal plume.

For detailed specifications of each measurement instrument, please refer to Table 2. Comprehensive information on test conditions can be found in Section 2.2.2.

2.2.2. Test conditions and measurement points

The measurements were executed October 27th, 2023, spanning from 07:00 AM to 09:00 PM. During this timeframe, the pump consistently operated under a constant flow regime (1.20 m^3/h), and the storage water heater maintained a steady temperature.

In Part 1 of the experiment, aligned with the available equipment and the study's objectives, temperature and velocity were observed in three vertical planes (V1-V3), four horizontal planes (H1-H4), and seven longitudinal planes (L1-L7), respectively in the x, z, and y directions, as depicted in Fig. 4-a to Fig. 4-c. The V1 to V3 planes are positioned at x = −55 mm, x = 0 mm, and x = 55 mm, respectively. The H1 to H4 planes are located between z = 2 023 mm and z = 2 923 mm, spaced 180 mm apart. The longitudinal planes were positioned midway between the first and last element of each radiator, with the L4 plane situated in the middle between the two radiators, referred to as RAD1 and RAD2 from now on. The intersection of the vertical and longitudinal planes results in a total of 21 points, and measurements for the horizontal planes were taken at each of these points, totaling 84 measurement points overall. Data acquisition for each point was continuous for 5 min at a sampling

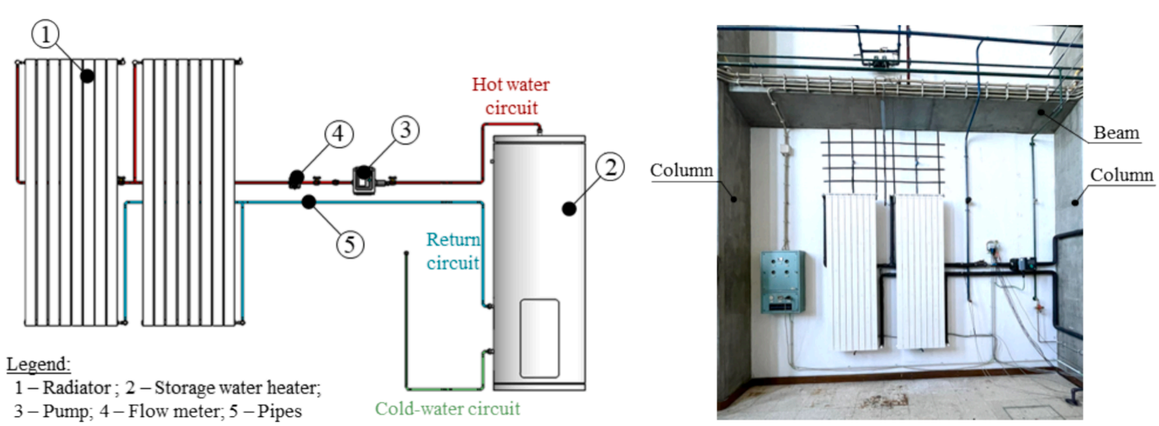

Fig. 2. Layout of the experimental installation.

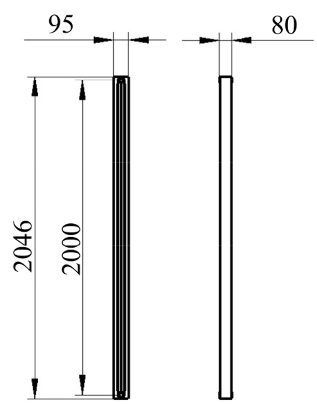

(a)

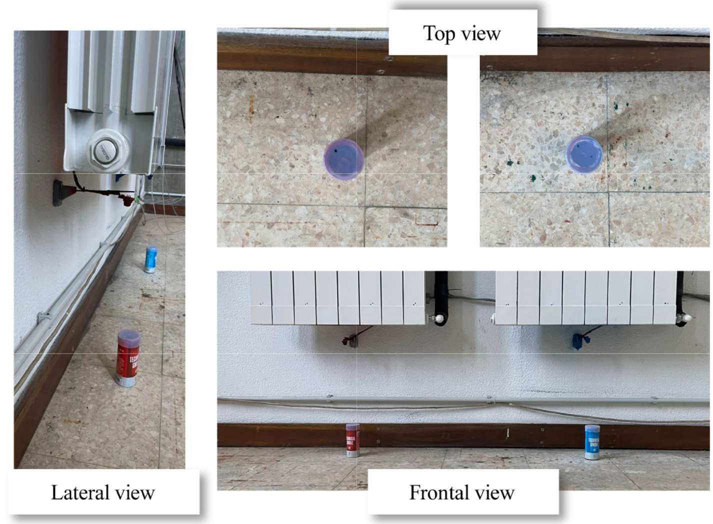

(b)

Fig. 3. Specifications for: (a) 1 radiator element, (b) location of technical smoke sources.

Table 1
Characteristics of 1 element of radiator.

Variable		Value
Dimensions	Overall height	2 046 mm
	Width	80 mm
	Depth	95 mm
	Pipe centres height	2 000 mm
Heat output EN 442	ΔT = 50 °C	321 W
	ΔT = 30 °C	161 W
Material		Diecast and extruded aluminium

rate of 1 s. The inlet and outlet water temperatures were monitored at a point in the piping shared by both radiators, with a sampling rate of 1 s. Additionally, the surface temperature of the radiators was examined at four points (Fig. 4-d), with each point undergoing three thermographic measurements.

In Part 2 of the experiment, one smoke source is positioned at the center of each radiator, and images are captured from three perspectives to document the smoke propagation. This part comprises a scenario where the smoke sources are placed beneath the radiators without grid (Fig. 4-e-w/o grid) and another scenario with a grid (Fig. 4-f-w/ grid). The use of the grid aims to minimize the effect of the initial velocity of the smoke sources. This is done to examine the impact of this velocity on visualizing the development of the thermal plume.

2.3. Numerical simulation

To model the thermal plumes generated by the radiators, the STAR-CCM+ software was employed [61], utilizing the finite volume method (FVM) for solving the fundamental equations governing fluid mechanics and heat transfer.

The CFD methodology utilized in this study is outlined in Fig. 5. The methodology consists of two steps, where in Step 1, two parallel models are created. Firstly, a 1/2-Element Model of the radiator was developed, covering all three regions (liquid, solid, and gas). At least six simulations were performed across the desired operating range of the installation to derive the convection coefficient (h), and the viscous and inertial resistance coefficients (K_v and K_i). Secondly, a 1- Element Model of the radiator was established, focusing solely on the solid region. This model underwent a temperature variation to ascertain the equivalent conductivity of the material in each direction, which would be utilized in the Simplified Model. For this step, the results presented in Table 3 are utilized.

In the subsequent stage, Step 2, a model termed as the Simplified Model was developed, wherein the radiators are modelled using the porous media (PM) approach. This simplification, specifically referring to the geometry of the radiators, allows for the representation of the 16 radiator elements, distinguishing them from the detailed geometric models used in Step 1, hence the designation of this model as simplified. This simplified model incorporates the properties from Step 1 and underwent validation based on experimental temperature and velocity results. The details of the model geometries are presented in Fig. 6, and a

Table 2
Specifications of measuring equipment.

Equipment		Range		Accuracy	Resolution
		Min	Max		
Humidity and temperature data logger	Humidity (%)	0	100	±1.5	0.01
	Temperature (°C)	−30	70	±0.2	0.01
Thermocouples DS18B20	Temperature (°C)	−55	125	±0.5	0.001
Thermo-anemometers (Van probe)	Velocity (m/s)	0.3	35	±(0.1 m/s + 1.5 % of mv*) (0.3 to 20 m/s)± (0.2 m/s + 1.5 % of mv*) (20 to 35 m/s)	0.01
	Temperature (°C)	−20	70	±0.5	0.1
Thermal Camera	Temperature (°C)	0	350	–	0.1
Smoke sensor	Concentration (ppm)	200	10,000	–	1
Camera	fps	60		–	–

*mv corresponds to the measured value.

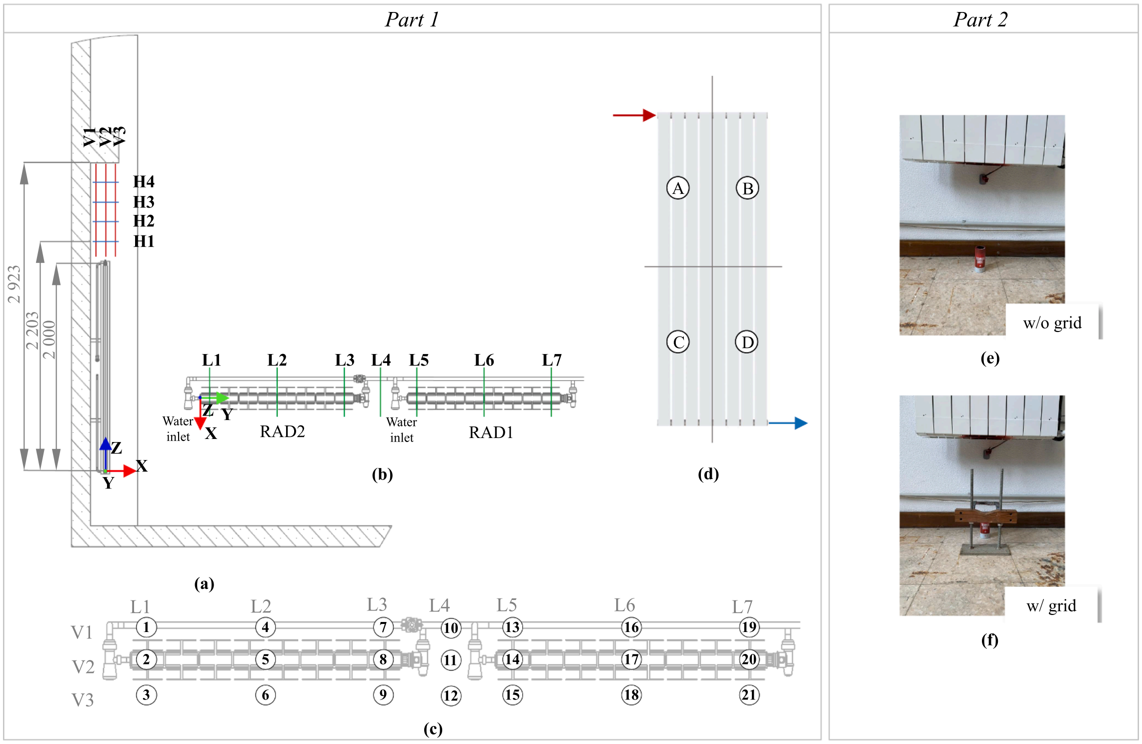

Fig. 4. Part 1 – Temperature and velocity measurement's locations: (a) above installation, (b) along length of two radiator, (c) measured points in each plane H; (d) Surface temperature points; Part 2 – Smoke: (e) source without grid, (f) source with grid.

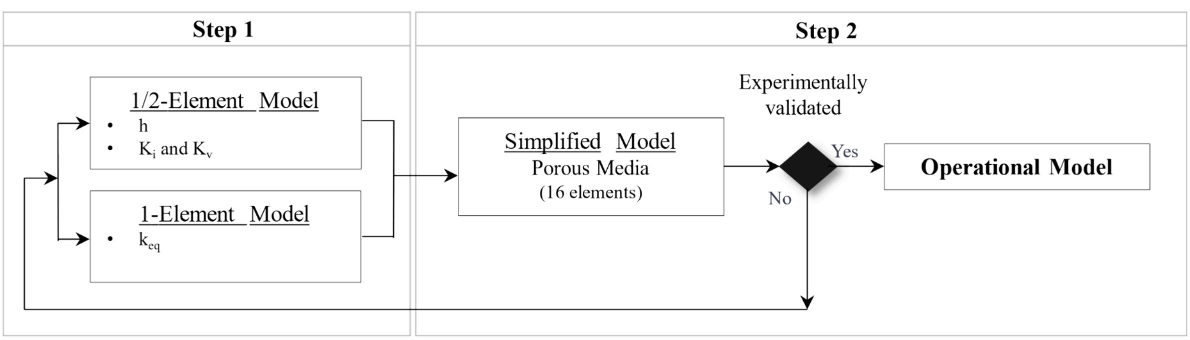

Fig. 5. CFD methodology.

Table 3
Heat transfer coefficient for radiators (W/m^{2}K).

Flow per element (m^3/h)	Inlet temperature (°C)		
	75	55	35
0.09	9.3	8.3	6.9
0.03	9.4	8.4	7.1
0.01	10.7	9.8	8.5

complete description of the CFD methodology can be found in the authors' reference [62].

2.3.1. Governing equations and models

The investigation utilized governing equations for three-dimensional, turbulent, and incompressible flow, employing the STAR-CCM+ commercial software [61]. Heat transfer in the radiator's water channels, driven by forced convection, was simulated as hot water circulated. Heat conducted through the radiator panels, heating the surrounding air, leading to natural convection modelled with the Boussinesq approximation. Radiation heat loss was accounted for using the surface-to-surface (S2S) model. Unsteady-state models with a time step of 0.01 s were employed. The mass, linear momentum, and energy conservation equations were solved using the SIMPLE algorithm for the pressure–velocity coupling, with mass, momentum and energy equations solved independently. Pressure correction was achieved through a predictive-corrective model. The software solved these equations by integrating over the control volume after discretizing the domain.

Turbulence effects were addressed using the RANS model, specifically the Realizable k-ε Two-Layer turbulence model, consisting of equations for turbulent kinetic energy and turbulence dissipation rate. The flow was assumed fully turbulent, rendering molecular viscosity effects negligible due to turbulent diffusion. Turbulent viscosity was expressed as a function of k and ε (Eq. (11)). Equations (12) and (13) outlined turbulent kinetic energy and its dissipation in the Standard k-ε model. The Realizable k-ε Two-Layer model shares equations with the Standard k-ε model but distinguishes itself by employing an all-y+ wall treatment approach, incorporating different formulations for k and ε in the inner layer near the wall.

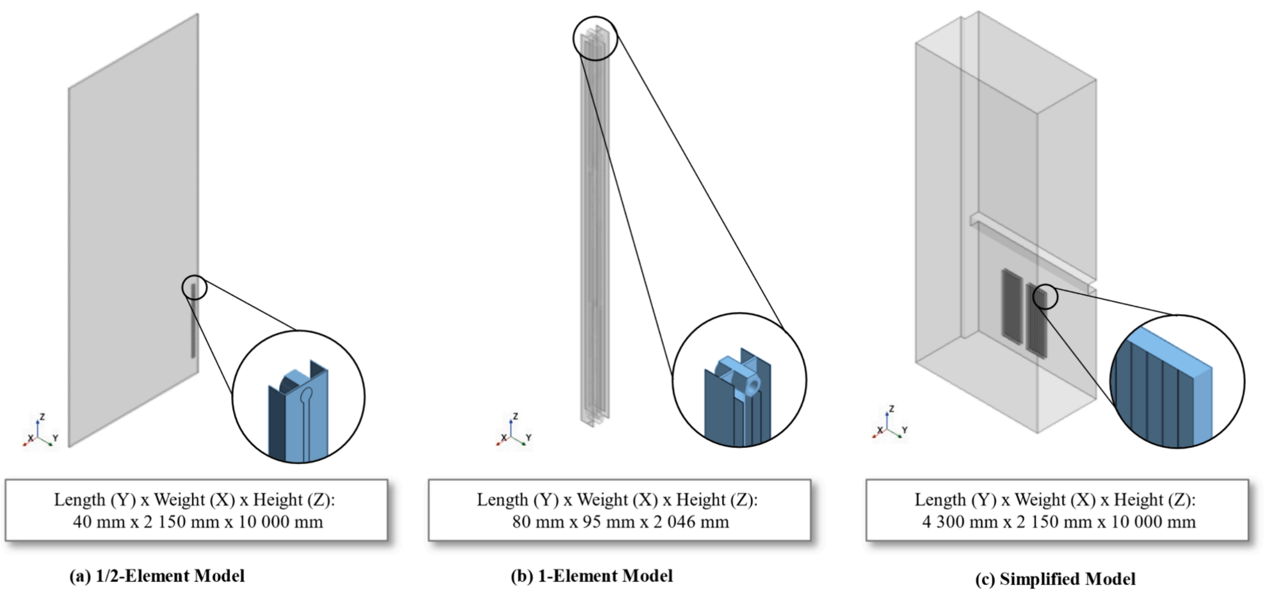

Fig. 6. Dimensions and geometrical details of the computational domains for Step 1 and Step 2.

$$\mu_t = \frac{\rho C_\mu k^2}{\varepsilon} \tag{11}$$

$$\frac{\partial}{\partial t}(\rho k) + \nabla\cdot\left(\rho k \underline{v}\right) = \nabla\cdot\left[\left(\mu + \frac{\mu_t}{\sigma_k}\right)\nabla k\right] + P_k - \rho(\varepsilon - \varepsilon_0) + S_k \tag{12}$$

$$\frac{\partial}{\partial t}(\rho \varepsilon) + \nabla\cdot\left(\rho \varepsilon \underline{v}\right) = \nabla\cdot\left[\left(\mu + \frac{\mu_t}{\sigma_\varepsilon}\right)\nabla \varepsilon\right] + \frac{1}{T_e}C_{\varepsilon 1}P_\varepsilon - C_{\varepsilon 2}\rho\left(\frac{\varepsilon}{T_e} - \frac{\varepsilon_0}{T_0}\right) + S_\varepsilon \tag{13}$$

In this context, C_μ is a dimensionless constant, $\underline{v}$ represents the mean velocity, μ is the dynamic viscosity, σ_k, σ_ε, $C_{\varepsilon 1}$ and $C_{\varepsilon 2}$ are constants specific to the model. P_k and P_ε are production terms, $T_e = k/\varepsilon$ is the large-eddy time scale, ε_0 is the ambient turbulence value in the source terms countering turbulence decay, T_0 is a specific timescale, and S_k and S_ε denote user-specified source terms.

The radiator's intricate geometry was simplified using a porous media (PM) approach, defining the PM as a solid allowing fluid passage. This approach modifies the equations governing flow and heat transfer, employing Darcy-Forchheimer's law. The law distinguishes two resistances: one viscous (resulting from friction stresses on walls) and the other inertial (from the flow profile) [63]. Porosity is a crucial parameter essential for solving the flow and heat transfer equations in the PM [61]. Further details can be found in reference [62].

The software used provides two porous media energy models: equilibrium and non-equilibrium. The equilibrium model assumes fluid and solid temperatures in the porous media are in equilibrium, suitable for fast thermal response times. In contrast, the non-equilibrium model allows for independent fluid and solid temperatures, accommodating slow thermal response times and significant thermal imbalances. In this study, the non-equilibrium model [61] was chosen for its better representation of reality, distinguishing between phases while maintaining their properties. In this model, the interaction area density is calculated as $A = A_{solid}/V_{solid}$ [64].

In summary, for applying porous media, key parameters include the heat transfer coefficient (h_t), interaction area (A) between phases, equivalent conductivity of the material (k_{eq}), water temperature profile, and resistance of the porous media ($P_v = \mu/K_v, P_i = \rho/K_i$). Experimental or numerical values can be used to determine P_v and P_i. Modeling the radiator as a parallelepiped porous media alters its shape, requiring the calculation of equivalent conductivity (k_{eq}). For radiators, heat flow in the x-direction was preferred, allowing for anisotropic conductivity of the solid phase. The water temperature profile, varying in height (coordinate z), was simplified based on inlet and outlet temperatures.

To represent smoke in the simulation, a passive scalar was employed. These scalars do not affect the physical properties of the simulation, and the transport Eq. for the passive scalar component ϕ_i is described by Eq. (14) [61].

$$\frac{\partial}{\partial t}\int_V \rho\phi_i dV + \oint_A \rho\phi_i v\cdot da = \oint_A j_i\cdot da + \int_V S_{\phi_i} dV \tag{14}$$

Where, i represents the component index, V is the volume, j_i denotes the diffusion flux, a is the area vector, S_{ϕ_i} is a source term for the passive scalar component i, and ϕ_i is assumed to be positive-definite.

2.3.2. Computational domain and boundary conditions

The computational domain utilized in numerical simulations is characterized by dimensions of 4 300 × 2 150 × 10 000 mm^3 (length × width × height). These model dimensions align with the testing room's size, yet constraints of 4 300 mm laterally and 2 150 mm frontally were applied due to the presence of other testing segments within the total volume. This geometric constraint specifically limits the available area, mainly influenced by the existence of isolated testing chambers.

The total computational domain, shown in Fig. 7, consists of two parts: the air part and the radiator part modelled by the porous media. The air part is characterized by the following boundary conditions: front and lateral surfaces are defined by a pressure outlet condition to ensure flow propagation. Since the actual size of the test room is larger than that of the domain, and there is an outflow of the flow (this reduction was implemented to optimize computational effort without compromising the development of the thermal plume, especially observed near the room's rear wall), the beam, column, top, and bottom surfaces are defined as insulated walls.

In the radiator part, the surfaces of the porous media are defined as walls, as the radiator surfaces at the contact interfaces are defined as baffle interface (surfaces of type number 13 – Fig. 7) to allow for radiation definition. The remaining radiator surfaces and spaces between elements are defined as internal interface to enable permeability of the surrounding porous media (surfaces of type number 10, 11, 12, and 14 – Fig. 7).

Regarding the boundaries of the smoke sources, all boundaries are defined as walls in the model validation simulation. Only the top

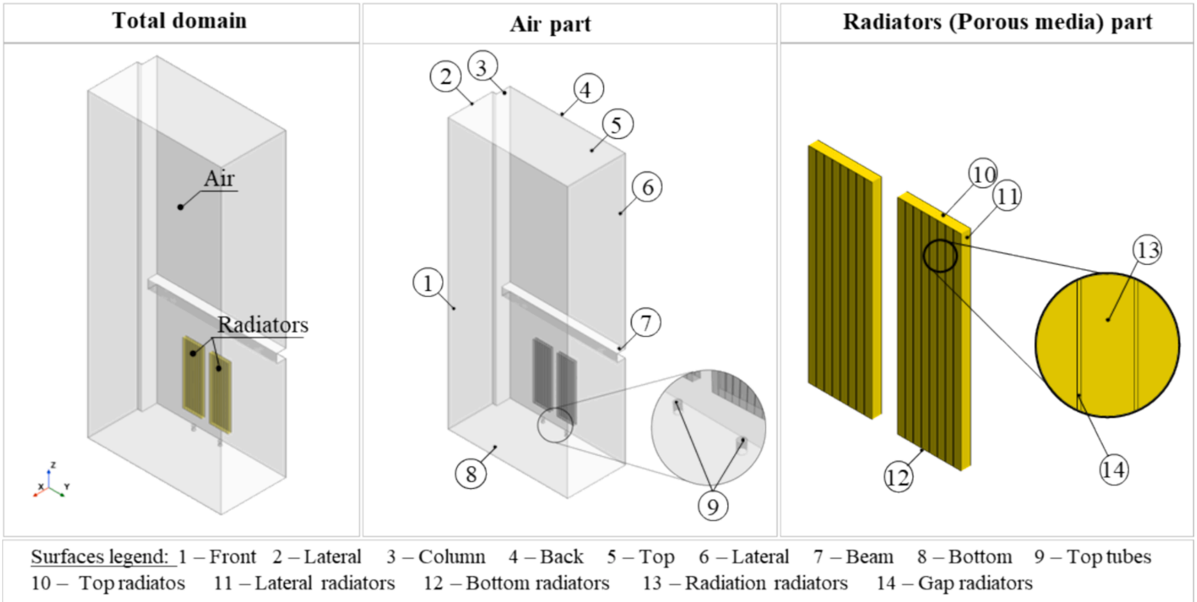

Fig. 7. Computational domain with identified parts and surfaces.

boundaries (number 9 in Fig. 7) are adjusted to velocity inlet for the simulation of the passive scalar representing smoke.

For this CFD model, the porous media was characterized based on the data provided in Table 3, incorporating an inertial coefficient of 2.34239 and a viscous coefficient of 5.7×10^{-4}, along with an air density of 1.2068 kg/m^3 and viscosity of 1.86×10^{-5} Pa-s. The equivalent conductivity of the radiator (k_{eq}) is specified as 15.28 W/mK in the x-direction, while preserving the original conductivity of the radiator material in the other directions. The porous media is identified by a porosity of 0.75 and an interaction area density of 494.6 /m.

Table 4 provides a comprehensive overview of the material properties used in the CFD model, covering air and Aluminum 3003-H12. The coordinate system used in the simulations aligns with that in the experimental measurements (Fig. 4), with a gravitational force of 9.81 m/s^2 applied in the negative z direction. Emissivity values for the room walls and radiator panels are set at 0.91 and 0.95, respectively [65]. Consequently, the only source of heat within the computational domain originates from the panel radiator.

Concerning the mesh utilized for the simulations, an isotropic mesh with polyhedral elements was generated, aiming to define control volumes and minimize the required number of elements for domain discretization. The model's mesh consists of 3 million cells, and the mesh dependency study included four meshes (from the course Mesh1 to the finer Mesh4). The study revealed that Mesh2 and finer exhibited relative errors below 0.03 % for outlet water temperature and 1 % for radiator heat output. This demonstrates that the simulation results maintained consistent accuracy and reliability across various mesh resolutions, thereby validating the meshing strategy employed in the study.

Table 4
Thermal properties of materials used in CFD models [60,66].

	Gas	Solid
Material	Air	Aluminum 3003-H12
Density (kg/m^3)	1.1740	2 730.0
Dynamic viscosity (Pa-s)	1.86E-5	–
Specific Heat (J/kgK)	1 003.6	893.0
Thermal Conductivity (W/mK)	0.03	163.0

3. Results and discussions

In this section, experimental results are showcased encompassing velocity and temperature fluctuations, complemented by images from smoke tests. The CFD model is validated, and the viability of employing a passive scalar for smoke simulation is examined. The analysis includes model validation, an exploration of how the initial velocity of the smoke source affects experimental thermal plume visualization, qualitative and quantitative comparisons between experimental and CFD visualizations, and an exploration of potential variations in experimental visualization angles of thermal plumes.

3.1. Model validation

To ensure simulation convergence, we managed residuals and monitored surface temperature and heat output of porous media. While there is no universally accepted method for assessing convergence, all simulations consistently demonstrated a progressive reduction in residuals, reaching a plateau and confirming convergence. In this study, all simulations utilizing an unsteady-state model (with a time step of 0.01 s) attained a significant reduction in residuals by 3–5 orders of magnitude.

In the validation process, the analysis begins with an examination of the experimental conditions. This includes the room air temperature and the evolution of inlet and outlet water temperatures for the radiators. Illustrated in Fig. 8, these temperature profiles span from 07:00 AM to 09:00 PM. The determination of an average ambient temperature is essential due to the non-controlled nature of the test environment, serving as a crucial input for the numerical simulation. In this study, the average ambient temperature was recorded as 22.16 °C, with a standard deviation of 0.47. For the inlet and outlet water temperature parameters (T_i, T_o), the average values were 68.19 °C and 63.67 °C, respectively. These parameters exhibited nearly constant evolutions throughout the measurement period. With a mean standard deviation of 0.69 °C for T_i and 0.47 °C for T_o, minimal variations were observed in both the inlet and outlet water temperatures. This consistency implies a stable and controlled heat transfer process within the installation.

For these experimental conditions, and through the application of Eq. (7), it was determined that the radiator's excess temperature above the indoor air temperature (ΔT) is 43.8 °C. The radiators are characterized by an average surface temperature of 55.1 °C, as measured at

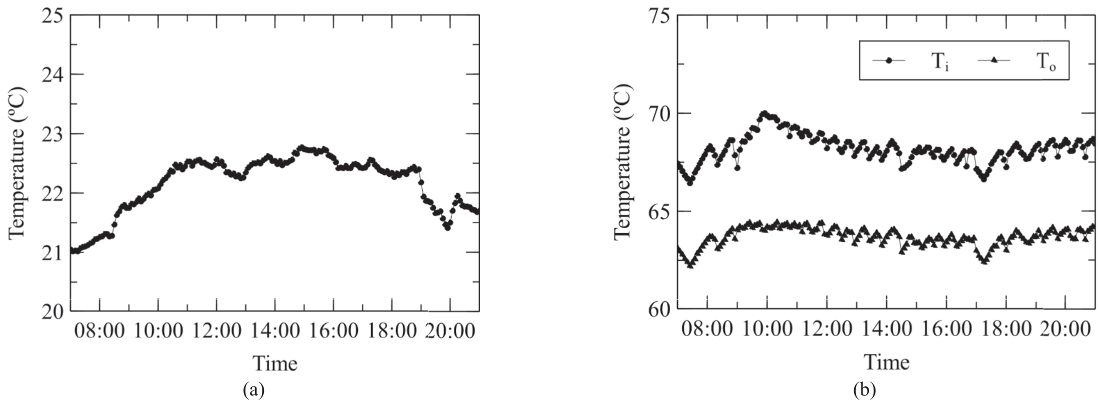

Fig. 8. Temperature evolutions: (a) room air (T_r) and (b) inlet and outlet water (T_i, T_o).

four points on each radiator (3 records per point), in accordance with the schematic representation in Fig. 4-d.

In Part 1 of the experiment, as described in Section 2.2.2, velocity and temperature parameters were monitored at 84 points around the periphery of the radiators, as illustrated in Fig. 4-a to Fig. 4-c. Fig. 9 depicts the corresponding measurements, with a distinction made for the four horizontal planes based on their height in meters (H1-black (2.203 m); H2-blue (2.383 m); H3-green (2.563 m); H4-white (2.743 m)). The average results from these four horizontal planes are used to validate the CFD model alongside the radiator's heat output and average surface temperature. The results are presented in Table 5, showing that for the exchanged heat, the relative error is only 4.2 %, a value lower than the typically accepted threshold of 10 %. Regarding the velocity parameter, the error varies between 0.7 % and 8.6 %, with the maximum value recorded for the H3 plane. For the temperature parameter, the relative error between the CFD and experimental models ranged from 4 % to 7 %, with the maximum value observed for the H4 plane. Concerning surface temperature, the CFD model's average based on the same points measured experimentally indicates a value of 58.8 °C, resulting in a relative error of 6.8 % compared to the experimental value. Since all relative errors for the parameters are below 10 %, the model is considered validated.

Finally, in Fig. 10, the distribution of temperature and velocity is presented in both the YZ plane and the XZ plane for both radiators (RAD 1 and RAD 2 – Fig. 2-b) at the midpoint of each radiator. Upon qualitatively analysing these distributions, it was possible to identify, for this study, the asymmetry of the profiles in both the longitudinal (x) and transverse (y) directions. These findings highlight the non-uniformity and asymmetry of the thermal plume development in both the YZ and XZ planes, and they will be further elucidated through the results of the smoke tests detailed in the following sections.

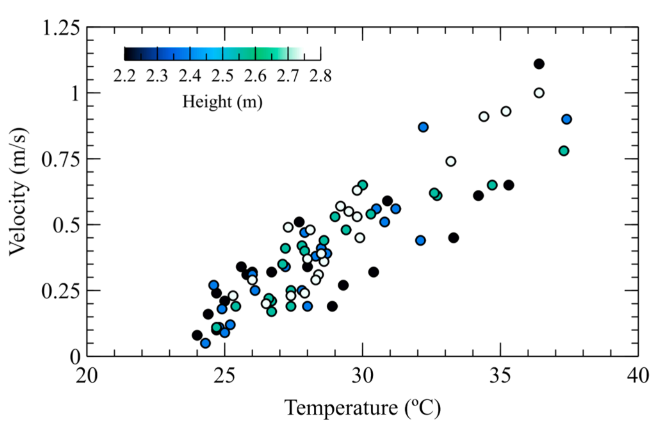

Fig. 9. Measurements of velocity and temperature at the periphery of the radiators.

3.2. Initial smoke source velocity impact

The smoke sources are activated by an ignition device to initiate smoke release, causing it to have an initial velocity different from zero. As the visualization of thermal plumes resulting from natural convection processes is investigated, it is crucial to examine the influence of this initial velocity on plume visualization and the potential impact it may have on its propagation.

Data obtained from experimental Part 2 was utilized to perform this analysis, as described in Section 2.2.2. In the first scenario of this part, smoke sources were positioned beneath the radiators without a grid, corresponding to the scenario where the initial velocity is higher. In the second scenario, a metal grid with 5 mm squares was placed above the smoke source to minimize the initial velocity of the smoke. The corresponding average initial velocity for both scenarios was determined using footage dedicated to the ignition region of the smoke sources. The obtained results demonstrated that the scenario without a grid is characterized by an average initial velocity (v_i) of 0.95 m/s, and the scenario with a grid by an average initial velocity of 0.22 m/s, representing an approximately 77 % reduction.

The impact of initial velocity on the visualization of thermal plume propagation was assessed by comparing frames at three different test durations (5 s, 40 s, and 80 s), as depicted in Fig. 11. This comparison considered colour intensities and the spatial location of these colours in the images, conducted through the study of similarity between two images in the thermal plume region using MATLAB. Similarity (Eq. (15)) is calculated based on the mean of Euclidean differences (Eq. (16)). Euclidean differences (Eq. (17)) are computed for each colour channel at every pixel. The closer the resulting similarity value is to 1, the higher the similarity between pixels and consequently, between thermal plume regions.

$$similarity = 1 - mean(d) \tag{15}$$

$$mean(d) = \frac{\sum_{i=1}^{M}\sum_{j=1}^{N} d_{ij}}{M \times N} \tag{16}$$

$$d_{ij} = \sqrt{\sum_{k=1}^{3}\left(Img1_{ijk} - Img2_{ijk}\right)^2} \tag{17}$$

Where $mean(d)$ represents the mean Euclidean difference, M and N are the dimensions of the images, and $Img1_{ijk}$, $Img2_{ijk}$ are the colour channel (R, G, B) values for pixels (i, j) in the images being compared.

To assess whether pixels outside the thermal plumes significantly contribute to the calculation of similarity (given its dependency on the

Table 5
Average velocity and temperature values for H1-H4 planes. For points measured see Fig. 4.

	T_o(°C)	Q (W)	Velocity (m/s)				Temperature (°C)			
			Plane							
			H1	H2	H3	H4	H1	H2	H3	H4
Experimental	63.67	4290.4	0.44	0.41	0.40	0.49	30.00	28.95	28.77	29.41
CFD	–	4469.5	0.44	0.43	0.44	0.47	31.82	30.19	30.31	31.47
Relative Error (%)	–	4.2	0.7	4.0	8.6	2.34	6.1	4.3	5.4	7.0

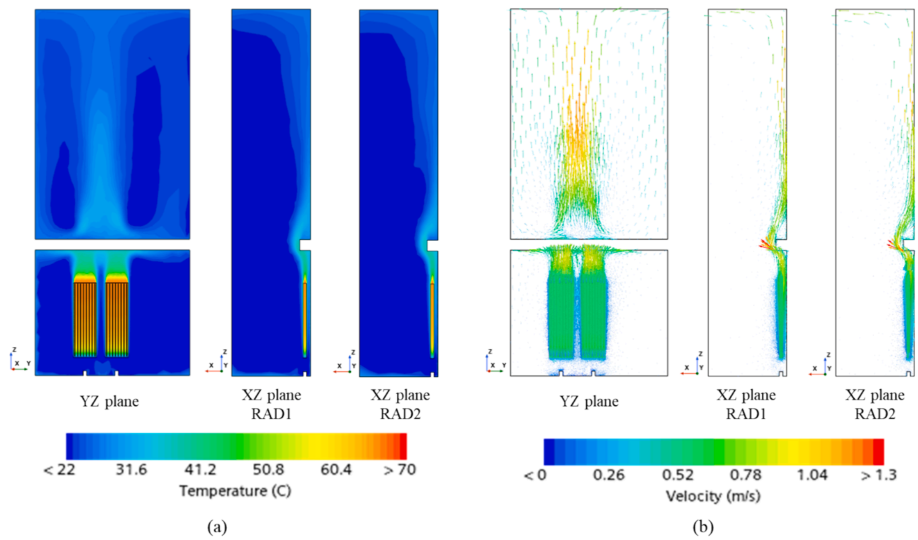

Fig. 10. Distribution in the YZ plane and XZ plane for RAD1 and RAD2: (a) temperature and (b) velocity.

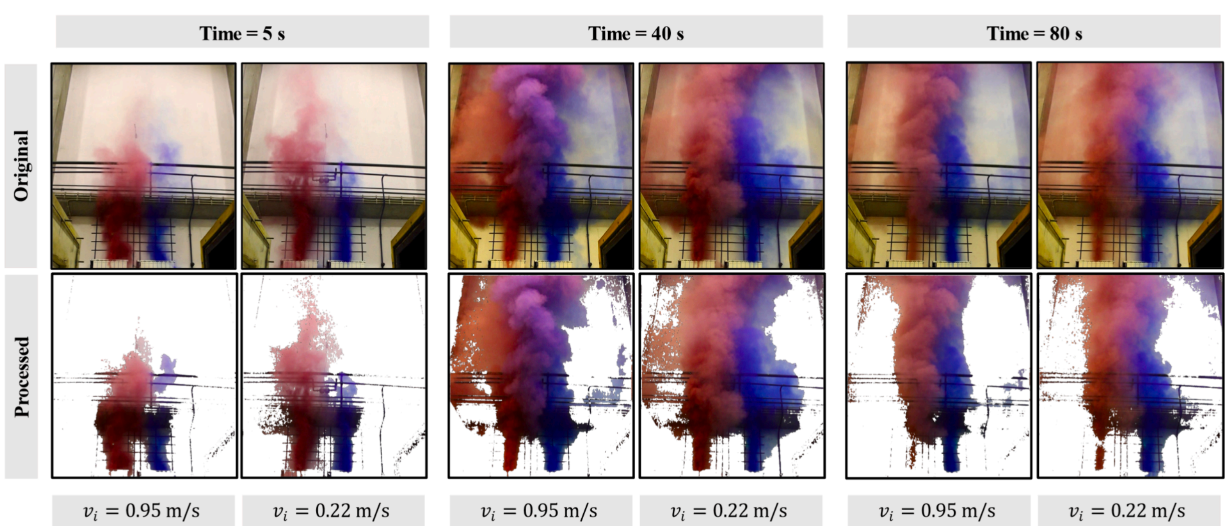

Fig. 11. Impact of initial velocity on the visualization of thermal plume propagation (scenario w/o grid – v_i=0.95 m/s; scenario w/ grid – v_i=0.22 m/s, see Fig. 4).

average of all pixels), thermal plume segmentation was performed using image processing. This involved filtering the smoke colours employed in the experiment (red and blue, as well as the mixing zone). The results of the image processing are depicted in Fig. 11.

By applying Eq. (15), it was possible to determine that, for the case of the original image, the similarity values were 0.87, 0.81, and 0.87 for the test durations of 5 s, 40 s, and 80 s, respectively. In the case of the processed image, with the segmentation of the thermal plume zone, the similarity values were 0.85, 0.78, and 0.85. Based on these results, it can be concluded that the segmentation of the thermal plume zone indeed allows for a determination of similarity free from the visual noise of other elements in the image, which impact the comparison, as it involves an average calculation, and these are fixed objects. The segmentation applies the same filters in both velocity scenarios. As expected, processed images yielded lower similarity values compared to the original case; however, they remained above 0.75 for all instances, indicating an acceptable level of similarity.

These similarity values also allow us to conclude that, for different time instances of the frames, the variation among them is less than 6 %. The calculated similarity values align with the qualitative analysis of

Fig. 11. Qualitative analysis demonstrates that between the two scenarios of initial velocity for the smoke sources, there are more significant variations in pixel colour intensity than in spatial location. This suggests that despite the initial velocity differing by approximately 77 %, the shape of the thermal plume remains similar, with the most visible difference occurring in the intersection zone of each radiator's plume. In this zone, the scenario with higher initial velocity exhibits greater mixing (purple hue is more pronounced) than the case with lower velocity. Considering these results, it can be concluded that minimizing the initial velocity of smoke sources is advisable to facilitate the visualization of the thermal plume, particularly in the intersection zone. However, if the goal is a global view of its development, it can be inferred that the initial velocity of the sources does not have a significant influence.

3.3. Qualitative validation of thermal plume propagation

Considering the previous results regarding velocity and its impact on the clarity of thermal plume visualization, an overlay was performed between experimental outcomes and numerical simulation results with the implementation of a passive scalar, as outlined in Section 2.3, with an initial velocity matching the determined experimental value and the respective location of smoke sources.

This overlay facilitates a qualitative comparison of experimental visualization with CFD Passive Scalar, validating the feasibility of using such smoke systems to investigate air propagation in large spaces with heat sources and confirming their suitability for qualitative validation of CFD models. The comparison utilized processed images in the YZ plane within a region limited by the presence of another test chamber in the testing room. While this comparison focuses on a single perspective, the following section will explore the potential of utilizing alternative perspectives for comparison.

In Fig. 12, the comparison is presented for the experimental case where the initial velocity of the smoke source is higher, v_i=0.95 m/s (scenario w/o grid – Fig. 4). This includes the original experimental image, the corresponding image of the CFD passive scalar, and their overlay highlighted in yellow to represent the passive scalar lines. It can be observed that, for all three-time instances, the simulation accurately represents the overall shape of the thermal plume. At 5 s, a correspondence in terms of the length of the thermal plume is evident between the experimental and CFD cases. At 40 s, an independent zone above the beam (see Fig. 2) is observed, with two ovals representing independent red and blue smoke areas, and in the middle, the mixing zone corresponds (purple colour) between the experimental and CFD cases. However, experimentally, lateral smoke dispersion is more visible than in the CFD, identified only by refining the passive scalar scale in that region. Finally, at 80 s, some correspondence in terms of the shape of the thermal plume is observed, and the independence of the thermal plumes from each radiator is visible in both the experimental and CFD cases. Notably, numerically, both smoke sources are synchronous, whereas in the experimental case, the blue smoke source had a slightly longer duration (less than 5 s). For all three instances, it is highlighted that, in the region below the beam, the passive scalar faithfully describes the lateral dispersion of smoke observed experimentally.

Similarly, in Fig. 13, the comparison is presented for the experimental case where the initial velocity of the smoke source is lower, v_i=0.22 m/s (scenario w/ grid – Fig. 4). This comparison also includes the original experimental image, the corresponding image of the CFD passive scalar, and their overlay highlighted in yellow to represent the passive scalar lines. It can be observed that, for all three-time instances, the simulation accurately represents the overall shape of the thermal plume. At 5 s, a correspondence in terms of the length of the thermal plume is evident between the experimental and CFD cases. At 40 s, an independent zone above the beam (see Fig. 2) is observed, where two ovals represent independent red and blue smoke areas, and the mixing zone is more visible than in the case presented in Fig. 12 since the smoke density is lower for the same instant. However, a slight lateral deviation of the blue smoke is observed in relation to the central position of the CFD. This is because an experimental deviation of the smoke was recorded, possibly due to some particles present in the composition of the smoke source that could not be controlled during the test. Finally, at 80 s, a correspondence in terms of the shape of the thermal plume is observed, and the independence of the thermal plumes from each radiator and their union are visible, both in the experimental and CFD cases. At this instant, the deviation of the blue smoke source was already smaller. It is emphasized that numerically both smoke sources are synchronous, while in the experimental case, as in the case with higher velocity, the blue smoke source had a slightly longer duration (also less than 5 s). In all three instances it is highlighted that in the region below the beam, the passive scalar faithfully describes the lateral dispersion of smoke observed experimentally.

Based on the results obtained for both velocities, the conclusions drawn from the qualitative comparison between experimental visualization and the CFD passive scalar model are crucial to validate the feasibility of employing smoke systems to analyse air propagation in large spaces with heat sources and to qualitatively validate CFD models.

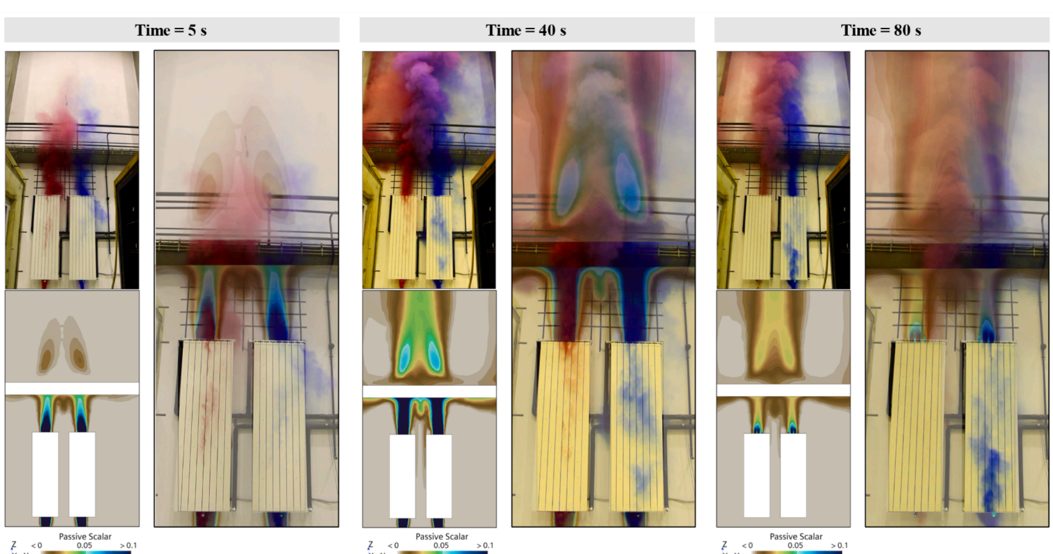

Fig. 12. Qualitative comparison of experimental visualization with CFD Passive Scalar: scenario w/o grid (v_i = 0.95 m/s), see Fig. 4.

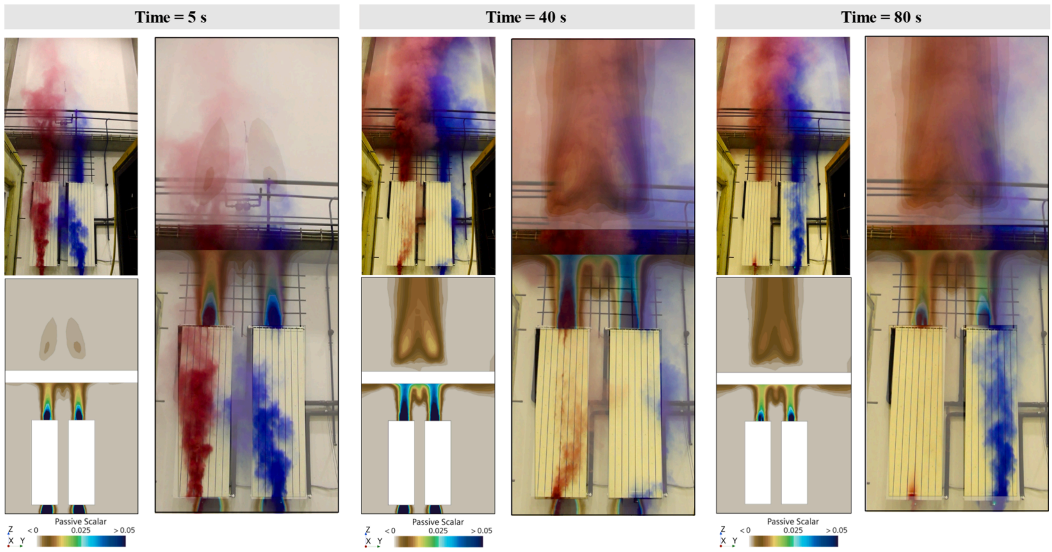

Fig. 13. Qualitative comparison of experimental visualization with CFD Passive Scalar: scenario w/ grid ($v_i = 0.22$ m/s), see Fig. 4.

The analysis revealed notable similarities in representing the overall shape of the thermal plume at different time instances, indicating that the CFD Passive Scalar model accurately captures the dynamics of air propagation in complex thermal environments. This method proved particularly effective in representing lateral smoke dispersion below the beam and the overall shape of the thermal plume, highlighting its viability for large-scale investigation. Observing variations in the dynamics of the thermal plume at different initial velocities of the smoke sources demonstrated the system's sensitivity to different conditions, enhancing the understanding of the impact of initial velocity on air propagation.

In the Fig. 14, average temperature, and velocity profiles in the three regions of the thermal plume were observed. As defined in Fig. 1 and described in Section 2.1, there are three zones. The profiles in Region 1 and Region 3 exhibit approximately Gaussian distributions, with Region 1 showing a profile for each heat source and Region 3 showing a single profile. The deviation from ideal Gaussian profiles is attributed to the determination for point heat sources, whereas in this case, the source is distributed. Additionally, in Region 2, the thermal plume begins to interact, evidenced by a deviation from Gaussian profiles characterizing the average buoyancy of a single plume. In this experimental scenario, the profiles are approximately Gaussian but not entirely, as theoretical concepts were devised for controlled ambient conditions and specific geometries. In this in-situ scenario, geometric disturbances (such as a beam) impact the development of the thermal plume and the temperature distribution on the panel, directly influencing velocity distribution and values, as previously observed by Calisir et al., 2016 [27].

In summary, the results reinforce the effectiveness of the approach, validating its applicability for researching complex thermal phenomena in large environments, and underscore the method's utility for qualitative validation of CFD models.

3.4. Quantitative validation of thermal plume propagation

To quantitatively validate the CFD model using the images resulting from the coloured smoke sources experiment, the CFD results of the passive scalar for the condition where the plume is fully developed, at 40 s, were used to determine the average values of the passive scalar within the thermal plume for the 3 regions of the plume, according to the horizontal lines presented in Fig. 15. For the scenario w/o grid ($v_i = 0.95$ m/s), a passive scalar value of 0.112, 0.073, and 0.042 was determined for regions 1, 2, and 3, respectively, and for the scenario w/ grid ($v_i = 0.22$ m/s), a passive scalar value of 0.025, 0.017, and 0.011 was determined for regions 1, 2, and 3, respectively.

To make the comparison, the smoke images were processed to standardize the blue and red tones to obtain an image where the two tones are more balanced and then normalized in terms of grayscale to determine the dimensionless smoke concentration by the maximum value of the scale used in the passive scalar. The representation of the concentration for the two velocity scenarios was presented in Fig. 15, and based on the location of the three regions, the average of the corresponding pixels was determined, resulting in a value for the scenario

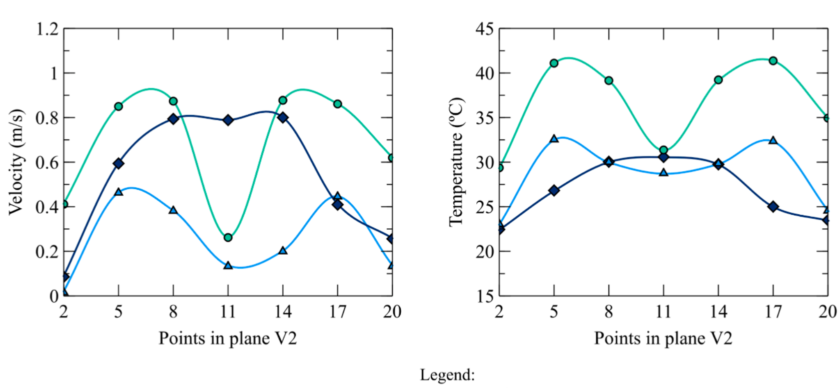

Fig. 14. Temperature and velocity profiles in the 3 regions of the thermal plume from CFD model. To view the points in the V2 plane, refer to Fig. 4.

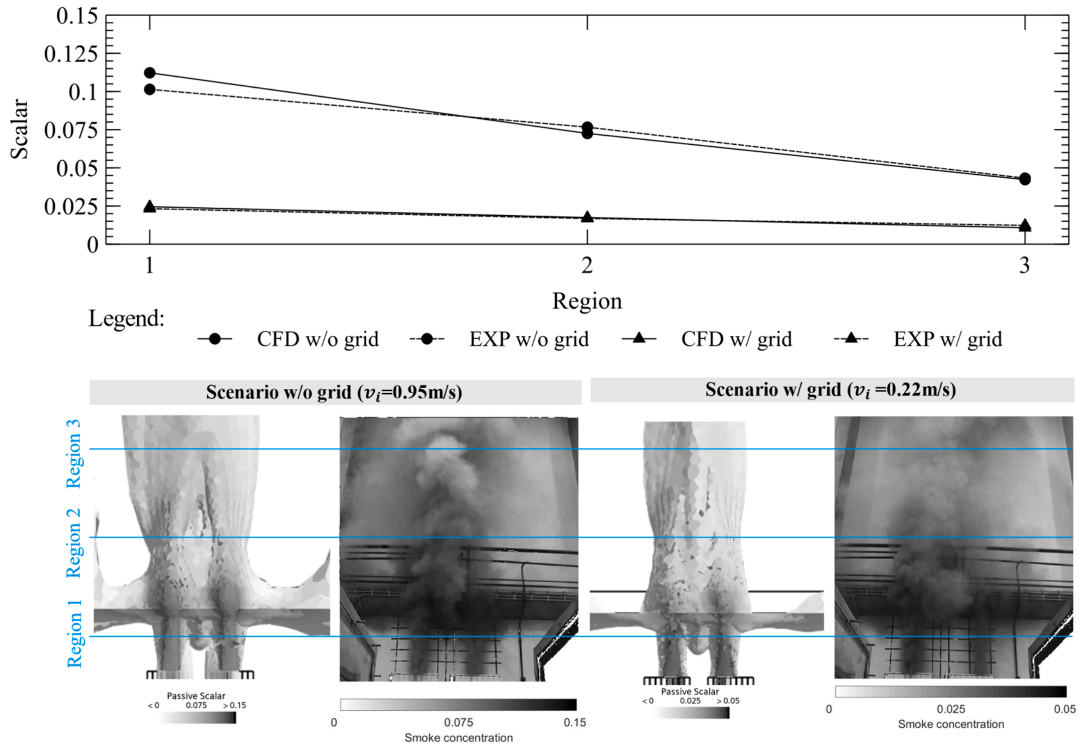

Fig. 15. Quantitative comparison of passive scalar and smoke concentration for the two initial smoke velocity scenarios.

w/o grid of 0.101, 0.077, and 0.043 for regions 1, 2, and 3, respectively, and for the scenario w/ grid, a value of 0.023, 0.017, and 0.012, for regions 1, 2, and 3, respectively.

Drawing upon the passive scalar value as a reference, we obtained relative errors spanning from 2.3 % to 14.5 %. Given the nature of this comparison rooted in smoke image processing, which inherently embodies dispersion, the attainment of relative errors below 15 % underscores the reliability of employing such metrics for quantitative validation while bolstering qualitative analysis. Thus, a way of validating the propagation of the wake was presented both in terms of the shape and the representation value of the smoke concentration.

To complement and substantiate the feasibility of utilizing of smoke systems for investigating air propagation in large spaces with heat sources and affirming their suitability for the qualitative validation of CFD models, the distribution of vortex sizes was evaluated through direct measurement of experimental vortices. This assessment aimed to establish their correlation with the integral length scale determined in the CFD model, considering the phenomenology of turbulence. The

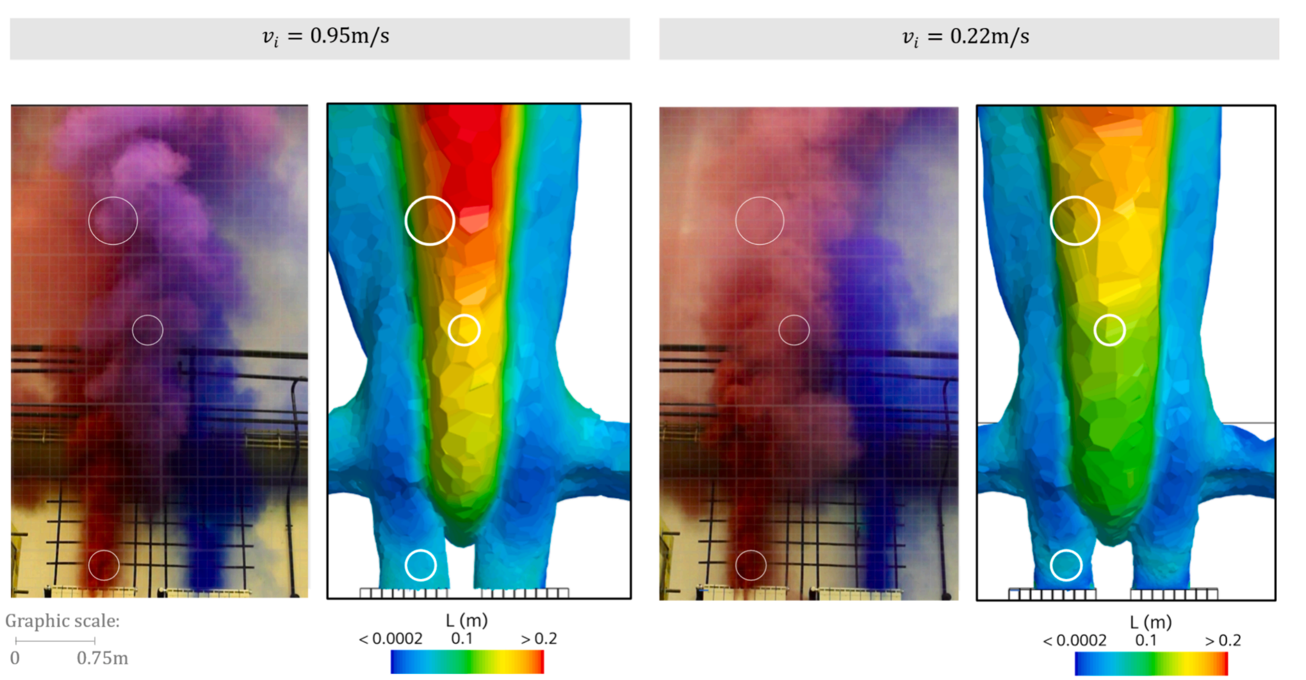

Fig. 16. Comparison of vortices experimental with CFD integral length scale (L) (scenario w/o grid – v_i=0.95 m/s; scenario w/ grid – v_i=0.22 m/s, see Fig. 4).

evaluation was conducted at the 40 s time instant, chosen for its heightened turbulence visibility in experimental observations.

To determine the direct dimensions of the vortices seen in the experimental images, three eddies were identified within approximately each region of the thermal plume, as highlighted in Fig. 16. The direct dimensions were determined using millimetre-scale measurement tools for analysing experimental imagery. For CFD results, the integral length scale was determined through the relationship between the dissipation rate of energy (ε) and turbulent kinetic energy (k) given by $\varepsilon \sim C_\varepsilon \times \left(k^{3/2}/L\right)$, where C_ε is a proportionality constant considered equal to 0.54 [61].

Qualitatively, as observed in Fig. 16, for both experimental cases with high and low initial velocity (scenarios w/o grid and w/ grid – Fig. 4), the spatial distribution of turbulence is similar within each radiator's thermal plumes and their mixing zones. In the experimental data, this is evident through the prevalence of red and blue smoke at the periphery of the thermal plume, corresponding to the zone of a smaller integral length scale, and the mixing of the two smokes resulting in a purple hue, corresponding to the region where turbulence dimensions are larger. For the case of lower initial velocity, it is observed that the mixing zone is less intense, indicated by the less pronounced colour of the smoke mixture. Quantitatively, relationship between the integral length scales in the CFD results for both tests in the three selected zones is of the same order of magnitude. Additionally, concerning the experimental data, the ratio between the direct dimensions of the vortices from the experimental images and the experimentally determined integral length scale corresponds to a ratio between 0.96 and 1.06 for the scenario without a grid and between 0.98 and 1.08 for the scenario with a grid. These values are very close to 1, indicating that the vortices are of the same order as the numerically determined integral length scale. The recorded values for the integral length scale range between 0.09 m and 0.19 m for the scenario w/o grid test (higher initial velocity) and between 0.06 m and 0.18 m for the scenario w/ grid test (lower initial velocity). Moreover, the values of the direct dimensions of the vortices from the experimental images are in the range of 0.06 m to 0.20 m for the scenario w/o grid test and from 0.08 m to 0.20 m for the scenario w/ grid test.

3.5. Application of plume visualization in perspectives

In Fig. 17 to Fig. 19, a qualitative comparison between experimental images and CFD results for views 1 to 3 is presented, respectively. When comparing the experimental images with CFD simulations from views 1 to 3, a significant consistency in the characteristics of the thermal plume was observed. This agreement indicates a strong correspondence between real observations and numerical representations of the model. The ability to capture the dynamics of the plume in three dimensions, especially when viewed from different angles, highlights the potential of coloured smoke sources as an effective tool for evaluating the dispersion of the plume in spaces with large air volumes.

This acceptable agreement between experimental perspectives and CFD simulations reinforces confidence in using these tools as valid means to investigate complex thermal phenomena. Moreover, it underscores the capability of coloured smoke sources to provide a comprehensive and accurate understanding of the thermal plume's behaviour under various conditions and orientations, including insights into the plume's development near structural elements (as demonstrated in View 3, allowing examination of the plume's development in proximity to the beam).

As shown, the results of this comparison demonstrate the utility of coloured smoke sources in conjunction with CFD for visualization studies and model validation, highlighting their applicability in researching air propagation in large spaces with heat sources.

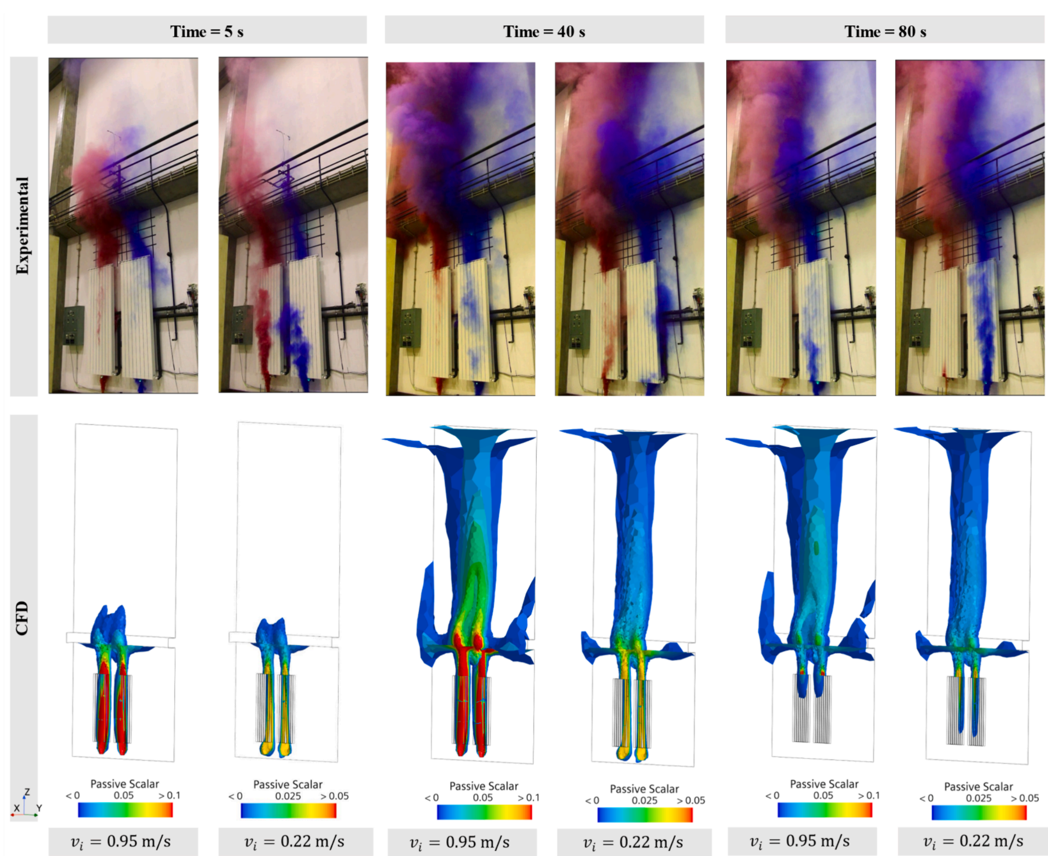

Fig. 17. Experimental e CFD results: View 1 (scenario w/o grid – v_i=0.95 m/s; scenario w/ grid – v_i=0.22 m/s, see Fig. 4).

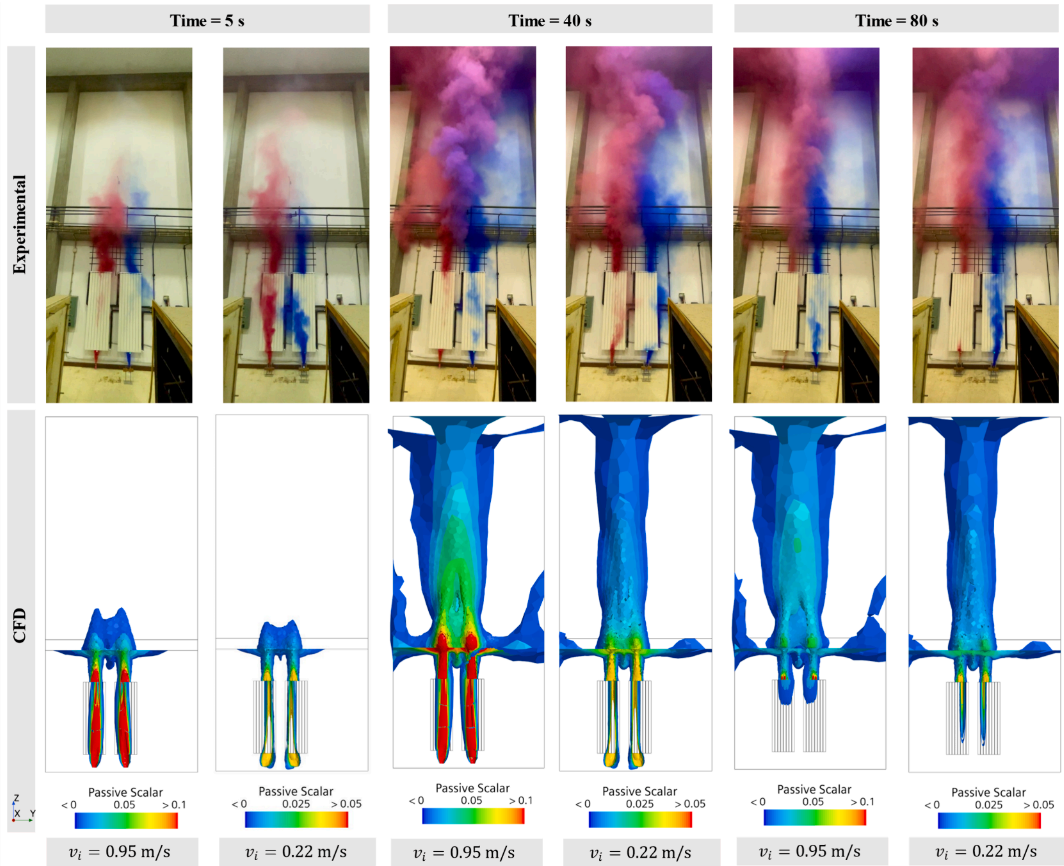

Fig. 18. Experimental e CFD results: View 2 (scenario w/o grid – v_i=0.95 m/s; scenario w/ grid – v_i=0.22 m/s, see Fig. 4).

4. Conclusions

This study examines the viability of employing coloured smoke sources to visualize thermal plume flow fields in (in-situ), naturally ventilated large spaces. It presents a way for both qualitative and quantitative validation of a CFD model using passive scalars to illustrate the propagation of the thermal plume, based on experimentally obtained images.

Experimental results demonstrated a high degree of correlation between measured air velocity, air temperature parameters, and corresponding values predicted by the CFD model in the 3 regions of thermal plume interaction. Relative errors for velocity, temperature, heat transfer and surface temperature were all below the commonly accepted threshold of 10 %, confirming the accuracy of the CFD model.

The detailed analysis of the similarity between the original and processed images made it possible to determine the impact of the initial velocity of the smoke sources on the visualization of the development of thermal plumes. The segmentation of the thermal plume zone, as presented in Fig. 11, effectively eliminated visual noise, and ensured a reliable determination of similarity. The calculated similarity values, for both original and processed images, indicated an acceptable level of similarity, with processed images exhibiting lower values, as anticipated.

Comparing similarity values for different time instances further reinforced the consistency of the results, with variations below 6 %. This alignment with qualitative analyses demonstrated that, despite a significant difference (approximately 77 %) in initial velocities, the shape of the thermal plume remained consistent, highlighting the robustness of the method.

The comparative analysis of experimental visualization with the CFD passive scalar model provided crucial insights, effectively capturing the dynamics of air propagation, particularly in lateral smoke dispersion below the beam and the overall shape of the thermal plume. The system's sensitivity to different initial velocities enriched the understanding of the parameter's impact on air propagation.

In the quantitative validation of the CFD model using images obtained from experiments with coloured smoke sources, the CFD results of passive scalar at the fully developed plume condition (at 40 s) were used to determine average passive scalar values within the plume's three regions. For scenarios with and without a grid, passive scalar values were calculated for each region. Smoke images were processed to standardize blue and red tones, followed by normalization in terms of grayscale to determine dimensionless smoke concentration. This allowed for comparison of concentration's representation between the two scenarios. Relative errors ranging from 2.3 % to 14.5 % were obtained, indicating the reliability of employing these metrics for quantitative validation and qualitative analysis of the wake propagation. Overall, this study provides a way for validating wake propagation in terms of both shape and smoke concentration representation.

In summary, this study not only demonstrated the effectiveness and applicability of using coloured smoke sources in conjunction with CFD to investigate complex thermal phenomena in large environments but also highlighted the utility of this approach for quantitative and qualitative validation of CFD models. The results suggest that minimizing the initial velocity of smoke sources is advisable for specific visualization objectives, while the overall impact on the global view of plume development is less significant. This study contributes valuable insights for future research in the field of air propagation in naturally ventilated spaces with heat sources, emphasizing the potential use of coloured smoke sources as a powerful tool for visualization and model validation studies.

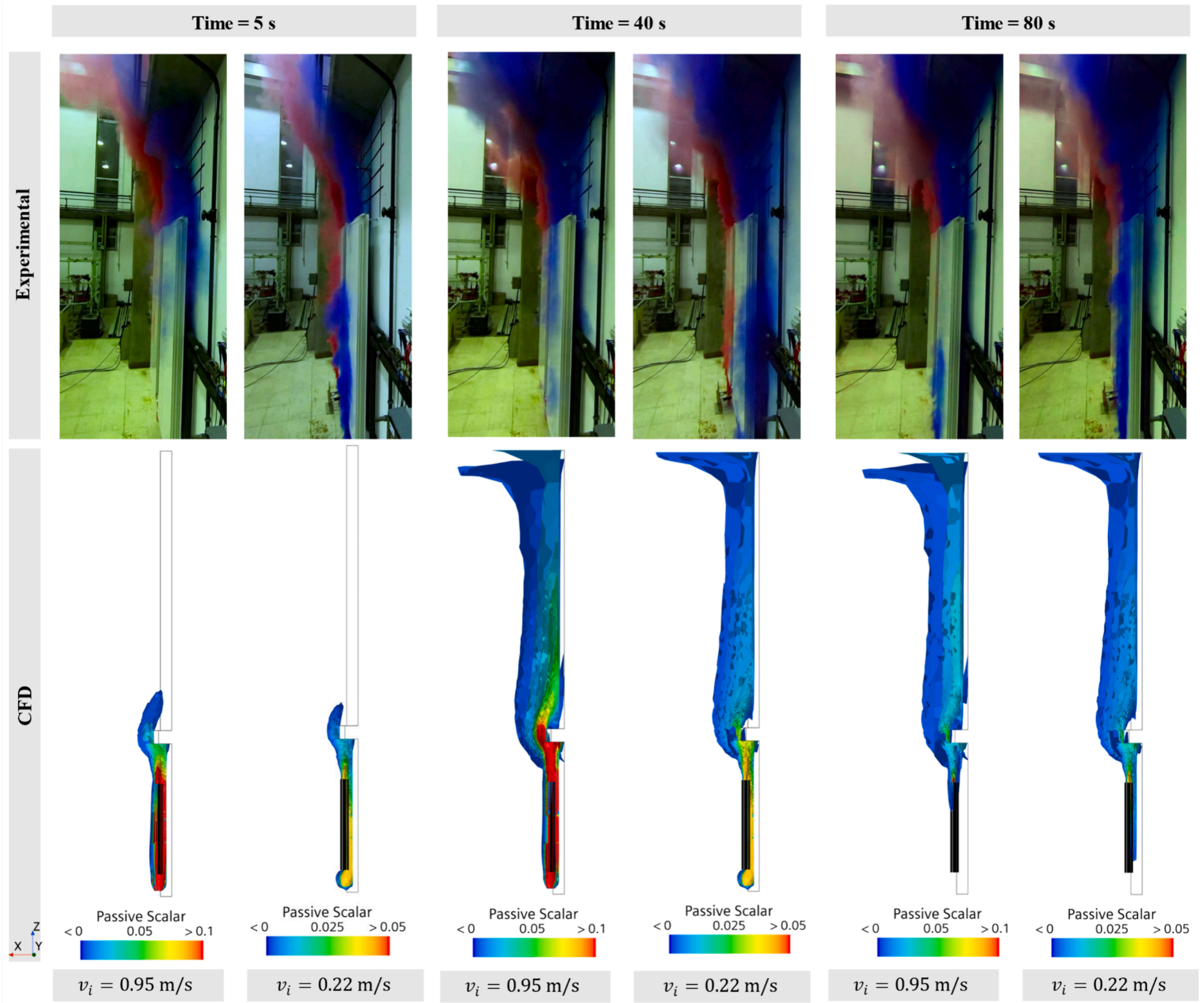

Fig. 19. Experimental e CFD results: View 3 (scenario w/o grid – v_i=0.95 m/s; scenario w/ grid – v_i=0.22 m/s, see Fig. 4).

CRediT authorship contribution statement

Rafaela Mateus: Writing – original draft, Validation, Software, Methodology, Investigation, Formal analysis, Data curation, Conceptualization. **Armando Pinto:** Writing – review & editing, Methodology, Funding acquisition, Conceptualization. **José M.C. Pereira:** Writing – review & editing, Supervision, Methodology, Funding acquisition, Conceptualization.

Declaration of competing interest

The authors declare that they have no known competing financial interests or personal relationships that could have appeared to influence the work reported in this paper.

Data availability

No data was used for the research described in the article.

Acknowledgements

The authors acknowledge Fundação para a Ciência e a Tecnologia (FCT) for its financial support via the project LAETA Base Funding (DOI: 10.54499/UIDB/50022/2020).

References

[1] R.C. Adhikari, M. Pahlevani, Characteristics of thermal plume from an array of rectangular straight fins with openings on the base in natural convection, Int. J. Therm. Sci. 182 (2022) 107798, https://doi.org/10.1016/j.ijthermalsci.2022.107798.

[2] D. Etheridge, A perspective on fifty years of natural ventilation research, Build. Environ. 91 (2015) 51–60, https://doi.org/10.1016/j.buildenv.2015.02.033.

[3] G. Carrilho da Graça, P. Linden, Ten questions about natural ventilation of non-domestic buildings, Build. Environ. 107 (2016) 263–273, https://doi.org/10.1016/j.buildenv.2016.08.007.

[4] A. Pinto, R. Mateus, J. Silva, M. Lopes, NZEB modular prefabricated building system, Sustain. Autom. Smart Constr. - Springer (2021), https://doi.org/10.1007/978-3-030-35533-3_20.

[5] European Commission, Can you afford to heat your home?, Accessed Febr. 2023, https//commission.europa.eu/news/can-you-afford-heat-your-home-2021-01-07_en. (2021).

[6] M. Pinto, F.M. da Silva, J. Viegas, V.P. de Freitas, Sistemas de Ventilação Natural em Edifícios de Habitação . Requisitos para a sua Modelização, Int. Conf. Eng. UBI2011 - Innov. Dev. (2011).

[7] C. Yang, L. Chen, T. Li, N. Lu, T. Gao, X. Gao, A. Li, Investigation of thermal plume and thermal stratification flow in naturally ventilated spaces with multiple heat sources, Build. Environ. 244 (2023), https://doi.org/10.1016/j.buildenv.2023.110754.

[8] C. Chen, C. Gorlé, Full-scale validation of CFD simulations of buoyancy-driven ventilation in a three-story office building, Build. Environ. 221 (2022) 17–21.

[9] Y. Liu, Y. Hu, Y. Xiao, J. Chen, H. Huang, Effects of different types of entrances on natural ventilation in a subway station, Tunn. Undergr. Sp. Technol. 105 (2020) 103578, https://doi.org/10.1016/j.tust.2020.103578.

[10] R. Mateus, J.M.C. Pereira, A. Pinto, Natural ventilation of large air masses : experimental and numerical techniques review, Energy Build. (2023) 113120, https://doi.org/10.1016/j.enbuild.2023.113120.

[11] T. Calisir, H.O. Yazar, S. Baskaya, Thermal performance of PCCP panel radiators for different convector dimensions – An experimental and numerical study, Int. J. Therm. Sci. 137 (2019) 375–387, https://doi.org/10.1016/j.ijthermalsci.2018.12.007.
[12] Y. Wang, A. Sergent, D. Saury, D. Lemonnier, P. Joubert, Numerical study of an unsteady confined thermal plume under the influence of gas radiation, Int. J. Therm. Sci. 156 (2020), https://doi.org/10.1016/j.ijthermalsci.2020.106474.
[13] M. Gomes, Avaliação das Taxas de Infiltração de Ar no Sector Residencial, MSc Thesis -, Univ. Coimbra, 2013.
[14] R.H. Hernández, Natural convection in thermal plumes emerging from a single heat source, Int. J. Therm. Sci. 98 (2015) 81–89, https://doi.org/10.1016/j.ijthermalsci.2015.06.010.
[15] J.S. Turner, Buoyancy effects in fluids, Cambridge Univ. Press, 1973 https://doi.org/10.1017/CBO9780511608827.
[16] A.R. Rahmati, A. Gheibi, Experimental and numerical analysis of a modified hot water radiator with improved performance, Int. J. Therm. Sci. 149 (2020), https://doi.org/10.1016/j.ijthermalsci.2019.106175.
[17] E. Aydar, I. Ekmekçi, Thermal efficiency estimation of the panel type radiators with CFD analysis, Isi Bilim. Ve Tek. Dergisi/ J. Therm. Sci. Technol. 32 (2012) 63–71.
[18] Q. Wu, Z. Wang, J. Dong, J. Liu, A method for judging the overheating of the radiator in the compensation of window downdraught based on thermal image velocimetry, Build. Environ. 197 (2021), https://doi.org/10.1016/j.buildenv.2021.107858.
[19] J.A. Myhren, S. Holmberg, Improving the thermal performance of ventilation radiators e The role of internal convection fins, Int. J. Therm. Sci. 50 (2011) 115–123, https://doi.org/10.1016/j.ijthermalsci.2010.10.011.
[20] S.M.B. Beck, S.C. Grinsted, S.G. Blakey, K. Worden, A novel design for panel radiators, Appl. Therm. Eng. 24 (2004) 1291–1300, https://doi.org/10.1016/j.applthermaleng.2003.11.026.
[21] T. Calisir, H.O. Yazar, S. Baskaya, Evaluation of flow field over panel radiators to investigate the effect of different convector geometries, J. Build. Eng. 33 (2021), https://doi.org/10.1016/j.jobe.2020.101600.
[22] T. Calisir, S. Baskaya, The influence of different geometrical dimensions of convectors on the heat transfer from panel radiators, SN Appl. Sci. 3 (2021) 1–16, https://doi.org/10.1007/s42452-021-04276-2.
[23] İ. Ekmekci, E. Aydar, A new design for panel radiators using CFD, Conf. Adv. Mech. Eng. ISTANBUL 2016 – ICAME2016. (2016).
[24] M. Embaye, S. Mahmoud, Thermal performance of hydronic radiator with fl ow pulsation e Numerical investigation, Appl. Therm. Eng. 80 (2015) 109–117, https://doi.org/10.1016/j.applthermaleng.2014.12.056.
[25] V. Chandak, S.B. Paramane, W.V. d Veken, J. Codde, Numerical investigation to study effect of radiation on thermal performance of radiator for onan cooling configuration of transformer, IOP Conf. Ser. Mater. Sci. Eng. Pap. 88 (2015), https://doi.org/10.1088/1757-899X/88/1/012033.
[26] P.M. Ferreira, M.A. Machado, M.S. Carvalho, P. Vilaça, G. Sorger, J.V. Pinto, J. Deuermeier, C. Vidal, Self-sensing metallic material based on PZT particles produced by friction stir processing envisaging structural health monitoring applications, Mater. Charact. 205 (2023) 113371, https://doi.org/10.1016/j.matchar.2023.113371.
[27] T. Calisir, H.O. Yazar, S. Baskaya, Determination of the effects of different inlet-outlet locations and temperatures on PCCP panel radiator heat transfer and fluid flow characteristics, Int. J. Therm. Sci. 121 (2017) 322–335, https://doi.org/10.1016/j.ijthermalsci.2017.07.026.
[28] A. Jahanbin, E. Zanchini, Effects of position and temperature-gradient direction on the performance of a thin plane radiator, Appl. Therm. Eng. 105 (2016) 467–473, https://doi.org/10.1016/j.applthermaleng.2016.03.018.
[29] R. Marchesi, F. Rinaldi, C. Tarini, F. Arpino, G. Cortellessa, M. Dell'isola, G. Ficco, Experimental analysis of radiators' thermal output for heat accounting, Therm. Sci. 23 (2019) 989–1002, https://doi.org/10.2298/TSCI170301168M.
[30] K. Võsa, A. Ferrantelli, T. Mall, J. Kurnitski, Experimental analysis of emission efficiency of parallel and serial connected radiators in EN442 test chamber, 132 (2018) 531–544. https://doi.org/10.1016/j.applthermaleng.2017.12.109.
[31] G.A. Ganesh, S. Lata, T. Nath, Numerical simulation for optimization of the indoor environment of an occupied office building using double-panel and ventilation radiator, J. Build. Eng. 29 (2020) 101139, https://doi.org/10.1016/j.jobe.2019.101139.
[32] D. Brandl, T. Mach, R. Heimrath, H. Edtmayer, C. Hochenauer, Thermal evaluation of a component heating system for a monastery cell with measurements and CFD simulations, J. Build. Eng. 39 (2021) 102264, https://doi.org/10.1016/j.jobe.2021.102264.
[33] T. Calisir, S. Baskaya, H.O. Yazar, S. Yucedag, Experimental and Numerical Prediction of Flow Field around a Panel Radiator, Conf. Environ. Renew. Energy. (2016).
[34] C. Cenedese, P.F. Linden, Entrainment in two coalescing axisymmetric turbulent plumes, J. Fluid Mech. 752 (2014) R2, https://doi.org/10.1017/jfm.2014.389.
[35] F. Durrani, M.J. Cook, J.J. Mcguirk, N.B. Kaye, B. Engineering, CFD Modelling of Plume Interaction in Natural Ventilation, Build. Simul. (2011) 14–16.
[36] C. Yang, A. Li, X. Gao, T. Ren, Interaction of the thermal plumes generated from two heat sources of equal strength in a naturally ventilated space, J. Wind Eng. Ind. Aerodyn. 198 (2020) 104085, https://doi.org/10.1016/j.jweia.2019.104085.
[37] F. Ciriello, G.R. Hunt, Analytical solutions and virtual origin corrections for forced, pure and lazy turbulent plumes based on a universal entrainment function, J. Fluid Mech. (2020), https://doi.org/10.1017/jfm.2020.225.
[38] J. Craske, M. Van Reeuwijk, Energy dispersion in turbulent jets. Part 2. A robust model for unsteady jets, J. Fluid Mech. (2015) 538–566, https://doi.org/10.1017/jfm.2014.669.
[39] J. Craske, M. Van Reeuwijk, Energy dispersion in turbulent jets. Part 1. Direct simulation of steady and unsteady jets, J. Fluid Mech. (2015) 500–537, https://doi.org/10.1017/jfm.2014.640.
[40] S. Yin, Y. Li, Y. Fan, M. Sandberg, Unsteady large-scale flow patterns and dynamic vortex movement in near-field triple buoyant plumes, Build. Environ. 142 (2018) 288–300, https://doi.org/10.1016/j.buildenv.2018.06.027.
[41] S. Yin, Y. Li, M. Sandberg, K. Lam, The effect of building spacing on near-field temporal evolution of triple building plumes, Build. Environ. 122 (2017) 35–49, https://doi.org/10.1016/j.buildenv.2017.05.030.
[42] S. Yin, Y. Li, Y. Fan, M. Sandberg, Experimental investigation of near- fi eld stream-wise fl ow development and spatial structure in triple buoyant plumes, Build. Environ. 149 (2019) 79–89, https://doi.org/10.1016/j.buildenv.2018.11.039.
[43] X. Gao, A. Li, C. Yang, Study on thermal stratification of an enclosure containing two interacting turbulent buoyant plumes of equal strength, Build. Environ. 141 (2018) 236–246, https://doi.org/10.1016/j.buildenv.2018.05.032.
[44] W. Von Funck, T. Weinkauf, H. Theisel, H. Seidel, Smoke surfaces: an interactive flow visualization technique inspired by real-world flow experiments, IEEE Trans. vis. Comput. Graph. 14 (2008), https://doi.org/10.1109/TVCG.2008.163.
[45] N. Gao, X.H. Liu, An improved smoke-wire flow visualization technique using capacitor as power source, Theor. Appl. Mech. Lett. 8 (2018) 378–383, https://doi.org/10.1016/j.taml.2018.06.010.
[46] M.Z.I. Bangalee, J.J. Miau, S.Y. Lin, J.H. Yang, Flow visualization, PIV measurement and CFD calculation for fluid-driven natural cross-ventilation in a scale model, Energy Build. 66 (2013) 306–314, https://doi.org/10.1016/j.enbuild.2013.07.005.
[47] A. John, K. Podila, Q. Chen, Y. Rao, Application of high-fidelity modelling approach to predict smoke and fire propagation in a nuclear fire scenario, 23 (2021) 1–10.
[48] A. Jiao, W. Lin, B. Cai, H. Wang, J. Chen, M. Zhang, J. Xiao, Q. Liu, F. Wang, C. Fan, Case Studies in Thermal Engineering Full-scale experimental study on thermal smoke movement characteristics in an indoor pedestrian street, Case Stud. Therm. Eng. 34 (2022) 102029, https://doi.org/10.1016/j.csite.2022.102029.
[49] X. Zhang, I. Reda, M. Aram, D. Qi, L. Leon, Scaling method between sub-scale helium and full-scale smoke tests of smoke spread during solar roof fires, J. Build. Eng. 70 (2023) 106426, https://doi.org/10.1016/j.jobe.2023.106426.
[50] X. Zhang, M. Aram, D. Qi, L.L. Wang, Numerical simulations of smoke spread during solar roof fires, 1 (2022) 561–570.
[51] H. Hu, H. Kikumoto, R. Ooka, C. Lin, B. Zhang, Comprehensive validation of experimental and numerical natural ventilation predictions based on field measurement with experimental house, Build. Environ. 207 (2022) 108433, https://doi.org/10.1016/j.buildenv.2021.108433.
[52] J. Chen, M. Zhong, P. Qiu, Z. Long, H. Cheng, A study of repeatability of hot smoke test in a subway station, Case Stud. Therm. Eng. 41 (2023) 102666, https://doi.org/10.1016/j.csite.2022.102666.
[53] C. Shi, J. Li, X. Xu, Full-scale tests on smoke temperature distribution in long-large subway tunnels with longitudinal mechanical ventilation, Tunn. Undergr. Sp. Technol. Inc., Trenchless Technol. Res. 109 (2021) 103784, https://doi.org/10.1016/j.tust.2020.103784.
[54] J. Wang, X. Kong, Y. Fan, X. Jiang, Reduced pressure effects on smoke temperature, CO concentration and smoke extraction in tunnel fires with longitudinal ventilation and vertical shaft, Case Stud. Therm. Eng. 37 (2022) 102311, https://doi.org/10.1016/j.csite.2022.102311.
[55] C. Viegas, P. Kaluzny, A. Durand, L. Fluchaire, D. Franco, P. Morais, Full-size experimental assessment of the aerodynamic sealing of air curtains for particulate matter, Build. Serv. Eng. Res. Technol. (2021), https://doi.org/10.1177/0143624420976400.
[56] P.F. Linden, G.F. Lane-Serff, D.A. Smeed, Emptying filling boxes: the fluid mechanics of natural ventilation, J. Fluid Mech. 212 (1990), https://doi.org/10.1017/S0022112090001987.
[57] P.F. Linden, The fluid mechanics of natural ventilation, Annu. Rev. Fluid Mech. 31 (1999) 201–238, https://doi.org/10.1146/annurev.fluid.31.1.201.
[58] EN 442-2, EN 442-2, Radiators and Convectors – Part 2: Test Methods and Rating, Com. Eur. Norm. (2015).
[59] R.S. John, R. Howell, M. Pinar Mengüc, K. Daun, Thermal Radiation Heat Transfer, 7.a ed.,, CRC Press, Boca Raton, 2020.
[60] Y. Cengel, M. Boles, M. Kanoglu, Thermodynamics - An Engineering Approach, 9.a ed.,, McGraw-Hill Education, New York, 2019.
[61] SIEMENS, Simcenter STAR-CCM+ Documentation - Version 2020.2, SIEMENS. (2020).
[62] R. Mateus, A. Pinto, M.C. Pereira, CFD methodology for predicting thermal plume from heat source: Experimental validation and simplified model, Build. Environ. 257 (2024), https://doi.org/10.1016/j.buildenv.2024.111526.
[63] N. Padoin, A.T.O.D. Toé, C. Soares, CFD Applied to the Investigation of Flow Resistances in Porous Media, Congr. Interam. Comput. Apl. a la Ind. Procesos. (2014).
[64] O.O. Noah, J.F. Slabber, J.P. Meyer, CFD Simulation of Natural Convection Heat Transfer from Heated Micro- Spheres and Bottom Plate in Packed Beds Contained in Slender Cylindrical Geometries, 6th Int. Conf. Porous Media, InterPore. (2014) 1–13.
[65] Thermoworks, Emissivity Table, Accessed on: December 2022, in https://www.thermoworks.com/emissivity-table/. (2023).
[66] MatWeb, Aluminum 3003-H12, Accessed on: December 2022, in https://www.matweb.com/search/DataSheet.aspx?MatGUID=5b30b87291e84c5e843a9b0025b7dfc6. (2022).